



Supplementary Materials for

Stochastic motion and transcriptional dynamics of pairs of distal DNA loci on a compacted chromosome

David B. Brückner *et al.*

Corresponding author: Thomas Gregor, tg2@princeton.edu

Science **380**, 1357 (2023)
DOI: 10.1126/science.adf5568

The PDF file includes:

Materials and Methods
Figs. S1 to S23
Tables S1 to S8
References

Other Supplementary Material for this manuscript includes the following:

Movies S1 to S7
MDAR Reproducibility Checklist

Materials and Methods

1	Experimental methods	3
1.1	Generation of the distance series	3
1.2	Microscopy	3
1.3	Nucleus and DNA locus segmentation and tracking	4
1.4	Chromatic aberration correction	5
1.5	Nucleus motion correction	7
2	Topological and transcriptional state analysis	8
2.1	Hidden Markov Model inference	8
2.2	Validating the HMM using simulated data	14
2.3	Single trajectory state analysis	15
2.4	Estimation of transcriptional lifetime	16
2.5	HMM parameter scaling analysis	19
2.6	Results without state splitting	22
2.7	Analysis of no- <i>homie</i> data	23
3	Analysis of single-locus dynamics	24
4	Analysis of two-locus dynamics	26
4.1	Two-locus MSD and relaxation time inference	26
4.2	Two-locus autocorrelation collapse	30
4.3	Velocity cross-correlations	30
5	Two-locus dynamics: theory	34
6	Comparison to mESC data	37
7	Code and software	38

1 Experimental methods

1.1 Generation of the distance series

The endogenous *eve* locus was tagged with MS2 stem-loops. First, an *attP* site was integrated at the first intron of *eve* using CRISPR-mediated homology-directed repair [72]. The two Cas9 cutting sites are marked in Fig. S1. Second, an *attB*-MS2 plasmid was used to deliver MS2 to the *attP* site. A genomic source of *phiC31* integrase (BDSC #34770) was used for the second injection. The synthetic *eve*-MS2 allele carries ~ 10.6 kb between the two Cas9 cutting sites.

A series of *attB* landing site lines were established by mobilizing the P-element construct P-2x*attB*-mW from a CyO balancer to the chromosome containing the *eve*-MS2 allele. A $\Delta 2$ -3 P-transposase line (BDSC #3629) was used for the transposition. Offspring displaying both Cy+ and w+ were subject to inverse PCR to map the location of the *attB* insertions. *attB* insertions at -3321.9, -589.3, +47.5, +77.5, and +179.3 kb from the *eve* promoter in cis are used in this study. Furthermore, in order to avoid the insertion biases of P-element, two MiMIC lines (MI02916 and MI00239, [73]) were recombined with the *eve*-MS2 chromosome to yield the -75.9 and -186.8 kb lines. The exact insertion points of these lines and their conversion to distances between the blue- and green-labeled spots are listed in Table S1.

Finally, the PP7 reporter transgenes (*parS*-*homie*-*evePr*-PP7 or *parS*-*lambda*-*evePr*-PP7) were integrated into the landing sites described above through recombination-mediated cassette exchange using BDSC #34770 as the integrase source. Transgenic flies with insertion orientations shown in Fig. S1A were obtained and used for the imaging experiments.

Fluorescent protein-tagged MCP, PCP, and ParB lines were made as previously described [8]. For maternal MCP::*3xmTagBFP2* and PCP::*3xmKate2*, a genomic landing site at 38F1 was used. For maternal ParB::*eGFP*, a landing site at 89B8 was used. All microinjections were performed as described previously [74].

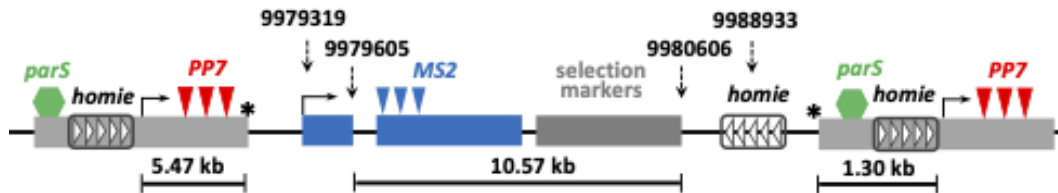


Figure S1: **Map of the genomic constructs.** The transcription start site (TSS) of *eve* (2R:9979319), the center of the endogenous *homie* element (2R:9988933) and the two Cas9 cutting sites (2R:9979605 and 2R:9980606, marked by stars) used for MS2 knock-in are labeled with dashed arrows. Each *evePr*-PP7 reporter line is named after the distance between its insertion site and the *eve* TSS, with a sign indicating upstream (-) or downstream (+) to the *eve* locus. Note that the new *eve* allele is larger than the endogenous one due to the presence of transgenic selection markers (GFP and RFP). The MS2-*parS* distance can be calculated from the distance shown below the map. Genomic distances and sizes of the sequence elements are drawn in scale.

1.2 Microscopy

Virgins carrying three fluorescent protein fusions (*yw*; MCP::*3xmTagBFP2*/PCP::*3xmKate2*; ParB::*eGFP*/+) were crossed with males containing the *eve*-MS2 allele and the *parS*-*evePr*-PP7 reporter transgenes. Embryos from the crosses above were dechorionated manually and mounted as described in [75].

Name	Breaking point on 2R	Distance to <i>eve</i> TSS (bp)	<i>MS2-parS</i> distance (kb)
-3322	6657453	-3321866	3327.7
-589	9389997	-589322	595.1
-142	9836454	-142865	148.7
-76	9903417	-75902	81.7
+47	10026855	47536	57.8
+77	10056812	77493	87.8
+179	10158620	179301	189.6

Table S1: **Details of the distance series.** All breaking point coordinates are from the Dm5 reference. Throughout the text, we cite the *MS2-parS* distances and refer to their rounded values in legends for simplicity.

A Leica SP5 confocal microscope with an oil immersion 63x NA 1.44 objective was used in all imaging experiments. Three laser lines at 405 nm, 488 nm, and 591 nm were used to excite mTagBFP2, eGFP, and mKate2, respectively. For each z slice, the emission channels for 405 nm and 591 nm were acquired simultaneously, followed by the 488 nm channel. Power measured at the objective for the 405 nm, 488 nm, and 591 nm lines was 0.4 μ W, 1.1 μ W, and 0.5 μ W, respectively. Three HyD detectors in photon counting mode were used to collect fluorescence emission spectra.

The voxel size for all images is 107x107x334 nm³ (x/y/z). The stack interval for all time-lapse videos was 28 s, except for the ones shown in Fig. 3C, 4B, and 4D, where the stack interval is 5.4s. For the data with a 28 s frame rate, an 8 μ m z-stack covering the whole nucleus along the apical-basal direction is acquired during the 28 s time interval. Images were taken at 1,024 x 256 x 25 voxels and focused on the posterior half of the embryo, encompassing *eve* stripes 3–7. Embryos were timed by their exit from mitosis 13 [76]. All embryos were imaged from 20 \pm 2 min to 55 \pm 2 min in cell cycle 14. Based on a localization control construct, the measurement errors in spot localization in this setup are 180 \pm 6 nm (mean \pm s.e.m.) [8]).

1.3 Nucleus and DNA locus segmentation and tracking

Segmentation and tracking of cell nuclei and DNA loci were done as described before [8]. Briefly, we computed the difference between the blue and red channels (since NLS::MCP::3x mTagBFP2 is enriched in the nuclear compartment while ParB-eGFP is enriched in the cytoplasm) by subtracting the maximum z-projection of the green channel from the blue channel, followed by Gaussian blurring ($\sigma = 5$) and binarization (local Otsu’s threshold at 5 x 5 μ m² [77]). To account for the motion of the whole embryo and the nuclei during imaging, we inferred the nuclear movement by minimizing the cross-correlation between nuclear masks of two consecutive frames. All nuclear segmentation and tracking results were scrutinized manually.

For DNA locus segmentation, we first identify candidate loci using sharpened raw image stacks from each of the three channels using a 3D bandpass filter (size 11 x 11 x 7 pixels), derived by subtracting a uniform filter from a Gaussian kernel ($\sigma = (1, 1, 0.6)$ pixel). All local maxima of this filtered image are considered candidate loci. At each local maximum, we constructed a cylinder mask with a diameter of 13 pixels (1.4 μ m) and a height of 7 pixels (2.3 μ m). We then set an intensity threshold such that the maximum number of candidate loci in the nucleus at each time point was less than 20, followed by

filtering the set of candidate loci using information on nuclear lineage, spot tracking, and the relative location of spot pairs.

For DNA locus tracking, we calculated the sub-pixel centroid of each candidate locus, only considering candidate loci located in the corresponding nuclear region obtained from the nuclear segmentation results. Spot tracking was then performed in three steps: a pre-tracking step, a gap-filling step, and a Bayesian filtering step [8].

1.4 Chromatic aberration correction

Imaging the positions of the *eve*-locus and the ectopic reporter with different wavelengths introduce chromatic aberrations, i.e. an instrumental error. This appears as a systematic error in our data (constant position displacements), which can vary across the field of view. Since positions of imaged loci are random, we assume that on average they have to be centered at zero, and any systematic errors are caused by the chromatic aberrations between the two channels. We perform a correction of this systematic error using data-driven and internally controlled (i.e., for the entire data set on any given day of data collection) calibration [8]. We consider the entire field of view and make a correction at each position in the 3D field of view.

We assume that the mean of the blue-green vector along each dimension is zero. For example, the probability that a blue spot appears above the associated green spot should be the same as the probability that it is below the associated spot. By applying linear regression to each dimension of displacements (x , y , and z) and extracting a 3x3 matrix, effectively the slope of this bias across the field of view in each dimension, the spot coordinates from a given color channel are scaled by the matrix to obtain the correction vector. This correction vector is the difference in the scaling of two channels, using one as a reference for the other to be matched to. Subtracting the correction vector from the original spot gives the corrected spot centroid, which can then be used for displacement calculation. This procedure effectively rescales the coordinates of all spots as to readjust the aberration slope across the fields of view to zero.

The assumptions underlying this approach were tested explicitly using control experiments with co-localized fluorescent proteins and three-color TetraSpec beads [8] (Fig. S2). This approach also allowed estimation of the residual measurement error in spot localization as being 180 ± 6 nm, in line with the errors inferred from our MSD analysis, see below (section 4.1).

Chromatic aberration correction was performed on a weekly basis, using all the embryos of the same genotype imaged over the week. An example of the correction is given in Fig. S2. We used this data-driven and internally controlled calibration scheme to estimate the blue-green distance for all genomic constructs, which we report in the main text.

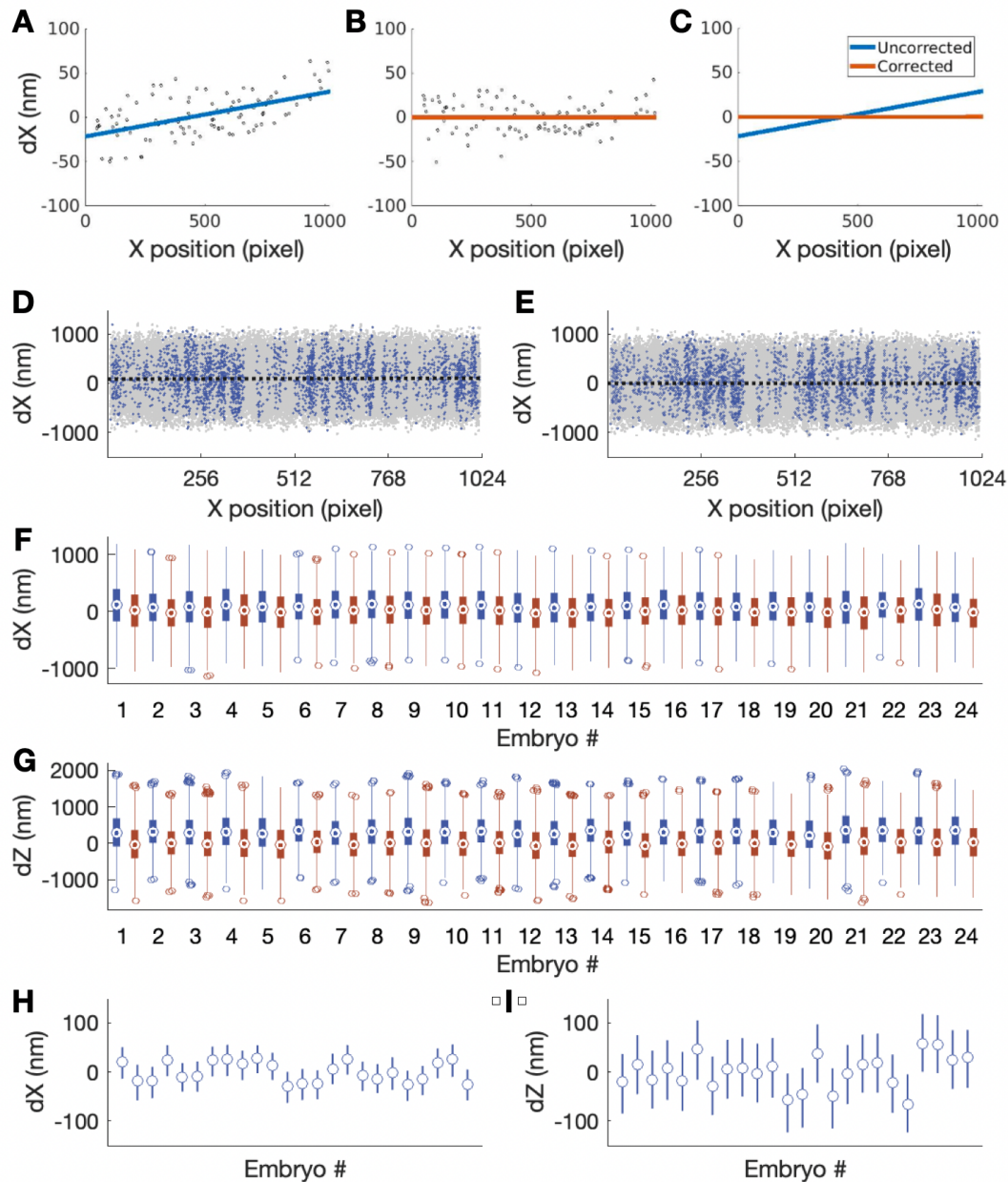


Figure S2: **Correcting chromatic aberrations.** (A-C) Chromatic aberration distance bias before (a) and after (b) correction with comparison (c) in the x -component of blue and green channels of calibration beads (Tetraspeck) for one image ($n = 95$). (D) A representative dataset showing raw *MS2-parS* distance, i.e. the raw distance between a blue-green spot pair (E-P distance) as a function of the spot pair position in the field of view (1 pixel = 107 nm). 24 *homie-evePr-PP7* embryos imaged over a week are included (gray points). These embryos form a chromatic aberration correction batch. Blue data points are from a single embryo. Dotted line shows the result of the linear fitting. The slope (0.0186 ± 0.0045) is significantly different from zero ($p = 3.96 \times 10^{-5}$, two-tailed t-test), indicating chromatic aberrations due to the optical setups. (E) E-P X distance after chromatic aberration correction described in Supplementary Methods. Both the slope and intercept are zero for the fitted line after the correction. (F, G) Boxplots showing distributions of the raw (blue boxes) and corrected (red boxes) E-P X (F) and Z (G) distance for each embryo in the correction batch. Medians are shown. Boxes represent the interquartile range, and the whiskers extend to 2.5 times the interquartile range above or below the medians. (H, I) Estimating errors associated with the correction. The errors are estimated by obtaining a correction matrix from every single embryo and applying it to all embryos in the same batch to get a distribution of the corrected E-P distance. Means of E-P distances calculated from the correction matrix derived from different single embryos are plotted, with bars showing 2.5–97.5 percentile range for dX (H) and dZ (I). The error (standard deviation) is 21 and 35 nm for dX and dZ, respectively.

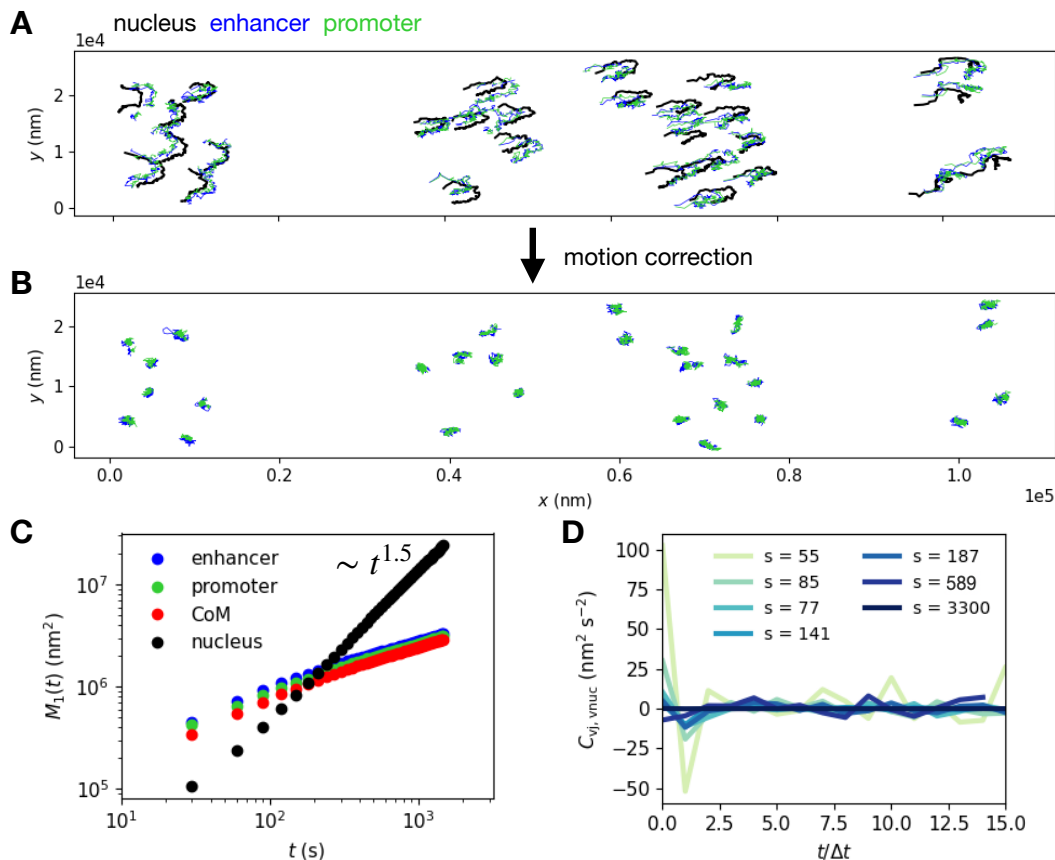


Figure S3: **Tracking of cell nuclei.** (A) Trajectories of nuclei (black), enhancer (blue), and promoter (green) within a single embryo ($s = 149$ kb) in the lab frame of reference. (B) Motion corrected DNA locus trajectories. (C) Single-locus MSD $M_1(t)$ (Eq. (S25)) of the enhancer (blue), promoter (green), their center of mass $(\mathbf{r}_1(t) + \mathbf{r}_2(t))/2$ (red), and the nucleus trajectories (black). Approximate scaling of the nucleus MSD is indicated. (D) Velocity cross-correlation of the motion-corrected locus trajectory and the nucleus trajectory, indicating no correlation beyond the first time point $t = \Delta t$, as expected for purely random measurement errors in the nucleus tracking (section 4.3).

1.5 Nucleus motion correction

Following tracking of the DNA loci, two further operations are performed: (i) we corrected for chromatic aberration to gain access to the dynamics of the 3D distance vector \mathbf{R}_{ij} ; (ii) we performed motion correction of the trajectories to obtain the absolute motion of DNA loci within the nucleus frame of reference.

To correct chromatic aberration, we perform a data-driven, internally controlled calibration; and approach that was tested extensively in previous work [8]. Briefly, we pooled raw instantaneous locus-pair distances across time, nuclei, and embryos, and analyzed the raw distances as a function of the locus-pair positions in the image field of view. To correct aberration, we applied a multivariate normal regression model to infer the correction matrix that allows the calculation of calibrated distances (see section above), which were used throughout the subsequent analysis.

To perform motion correction, we subtract the nucleus trajectories from the DNA locus trajectories (Fig. S3A,B). In many experimental systems, this is challenging as nuclei often undergo complex combinations of rotation, shape changes, and translation. During the final phase of the syncytial blastoderm stage of the developing *Drosophila* embryo, nuclei undergo very little relative motion, do not rotate,

and simply show affine global translation, which we can track as described above. As the same nucleus trajectory is subtracted from both DNA loci, measurement errors in the nucleus tracking could introduce spurious correlations in the observed relative motion of the two DNA loci. To exclude systematic measurement errors in the nucleus tracking, we calculate the velocity cross-correlation of the motion-corrected locus trajectory and the nucleus trajectory (Fig. S3D), which is consistent with the expectation for time-uncorrelated measurement errors in nucleus tracking (section 4.3). Furthermore, we find no traces of spurious motion in the trajectories of the DNA locus center of mass, as its MSD follows the same subdiffusive exponent as that of individual loci, which should be contrasted with the superdiffusive exponent of the nucleus movement (Fig. S3C). Together, these tests demonstrate that nucleus tracking and motion correction only introduces random time-uncorrelated measurement errors in the locus trajectories, which we account for using error correction in the velocity cross-correlations (section 4.3).

2 Topological and transcriptional state analysis

2.1 Hidden Markov Model inference

Based on the architecture of our genetic system comprising the enhancer and promoter, which are each flanked by a *homie* insulator element, the system can be in one of three states: (i) A state where the two *homie* elements are unbound, termed O_{off} . In this state, we expect large inter-locus distances. (ii) A topologically distinct state where the two *homie* elements are bound, but where transcription is inactive, termed P_{off} . In this state, we expect small inter-locus distances, and no signal in the red channel. (iii) A state where the two *homie* elements are bound and transcription is active, termed P_{on} . In this state, we expect small inter-locus distances, and the red channel to be on. The existence of these three states was demonstrated previously using various control experiments with individual elements of the genetic cassette missing [8]. To verify the assumption that active transcription corresponds to smaller physical distances in all sampled genomic separations, we plot interlocus distances depending on the intensity of the red channel (Fig. S4). This confirms that transcriptionally active states are associated with smaller physical distances, consistent with previous observations [8].

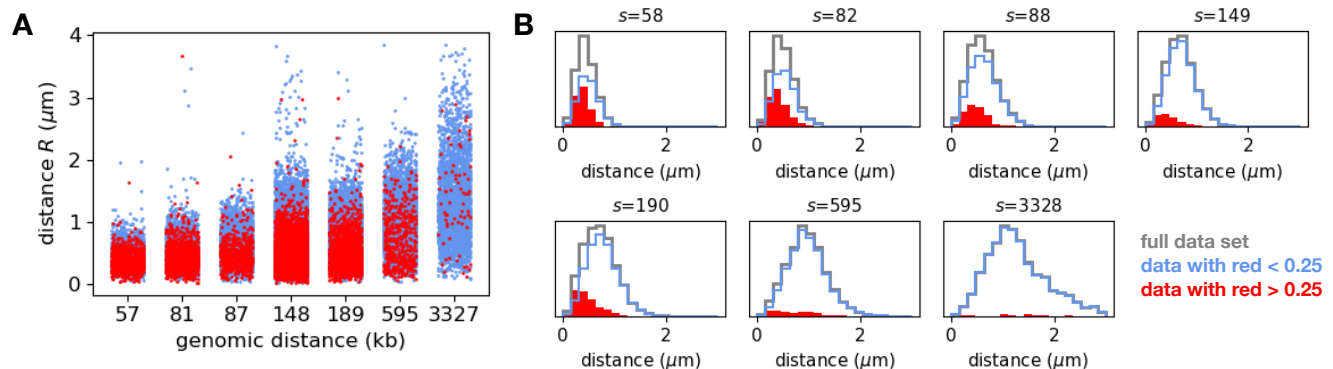


Figure S4: **Interlocus distances as a function of the transcriptional state.** (A) Scatter plots of the entire data set for each genomic separations, with points colored by whether the red signal is on (red intensity > 0.25 ; red), or off (red intensity < 0.25 ; blue). (B) Histograms of the interlocus distances for the entire data set (grey), points where the red signal is on (red intensity > 0.25 ; red), or off (red intensity < 0.25 ; blue).

Together, these arguments suggest an underlying structure of state transitions as shown in Fig. S5A. Transitions between O and P toggle between two distinct topological states; transitions between OFF

and ON toggle between two transcriptionally distinct states. Importantly, the details of the state inference performed here do not influence our later analyses on the polymer configurations or dynamics, which are based directly on the observed distance trajectories, which do not sensitively depend on the inferred underlying states (see Supplementary Section 2.6).

To infer the particular state of the system at each moment in time, we modeled the data (inter-locus distance and intensity time-series) as a Hidden Markov Model (HMM) [78] calibrated using a Markov Chain Monte Carlo (MCMC) sampler [79]. The general idea underlying ‘classical’ inference is to maximize the probability of the data under some model, namely to find the parameters Θ that maximize the likelihood of the data \mathcal{D} . In this manuscript we adopted a Bayesian approach, simultaneously estimating the state identity and the probability of the state transition rates given the observed data, i.e., the joint posterior distribution $P(\Theta|\mathcal{D})$, using Bayes’ rule:

$$P(\Theta|\mathcal{D}) = \frac{P(\mathcal{D}|\Theta)P(\Theta)}{P(\mathcal{D}) \equiv \int P(\mathcal{D}|\Theta)P(\Theta)d\Theta}, \quad (\text{S1})$$

where $P(\Theta)$ is the prior that encodes for prior knowledge about the parameter values, which we take to be log-uniform here since these are real, positive, and have some unknown scale [50].

The likelihood of the data $P(\mathcal{D}|\Theta)$ is expressed in terms of the likelihood of the individual nuclei time-series, which are independent:

$$P(\mathcal{D}|\Theta) = \prod_{i=1}^{N_{\mathcal{D}}} P(\mathcal{D}_i|\Theta), \quad (\text{S2})$$

where $\mathcal{D}_i = \{(R_0, R_1, \dots), (I_0, I_1, \dots)\}$ corresponds to the time series of the inter-locus distance R and the transcriptional fluorescence intensity I for a single nucleus. Assuming an HMM, the likelihood of a single nucleus takes the following form:

$$P(\mathcal{D}_i|\Theta) = \sum_{\{\Lambda\}} \left[\prod_{t=1}^{N_t} P(R_t, I_t|\lambda_t)P(\lambda_t|\lambda_{t-1})P(R_0, I_0|\lambda_0)P(\lambda_0) \right], \quad (\text{S3})$$

where λ_t is the hidden state of the system at time t (either O_{off} , P_{off} , or P_{on} , Fig. S5A), $P(R_t, I_t|\lambda_t)$ the ‘‘emission’’ probability, $P(\lambda_t|\lambda_{t-1})$ the transition probability, $P(\lambda_0)$ the initial state probability, and the sum is performed over all possible state configurations $\Lambda \equiv (\lambda_0, \lambda_1, \dots)$. The likelihood above is computed efficiently using the forward algorithm [78].

For our specific case, we modeled the emission probability that relates the data to the hidden states, as two independent probability distributions, i.e. $P(R, I|\lambda) = P(R|\lambda)P(I|\lambda)$. The first is the probability distribution $P(R|\lambda)$ for the inter-locus distance R_{ij} given each state λ . We find that the Maxwell-Boltzmann distribution provides a good fit to the experimental distributions of inter-locus distances (Fig. S5E). Therefore, we assume this general functional form for the distance distributions:

$$P(R_{ij}|\sigma_R) = 4\pi R_{ij}^2 \left(\frac{3}{2\pi\sigma_R^2} \right)^{3/2} \exp \left(\frac{-3R_{ij}^2}{2\sigma_R^2} \right). \quad (\text{S4})$$

This distribution is quantified by a single parameter σ_R , which is the average distance, i.e. $\langle R_{ij} \rangle = \sigma_R$. This is the probability distribution of end-to-end distances of an ideal chain polymer, with $\sigma_R^2 = Na^2$, where N is the number of monomers and a is the monomer length [54]. We choose this general functional form here as it simplifies the inference (single parameter) and also provides a good fit for our empirical observations.

The second distribution $P(I|\lambda)$ models the fluorescence I of the red channel (as a measure of transcriptional activity) conditioned on whether the state λ is transcriptionally active (P_{on}) or inactive (O_{off} or P_{off}). To capture the broad distribution of fluorescence intensities in the transcriptionally active state (P_{on}), we employ a Rayleigh distribution as an effective model to approximate the expected overdispersed Poisson noise due to transcriptional bursts and the additive Gaussian measurement noise :

$$P(I|\sigma_I) = \frac{I}{\sigma_I^2} \exp\left(\frac{-I^2}{2\pi\sigma_I^2}\right). \quad (\text{S5})$$

Importantly, this distribution remains simple as it is quantified by a single parameter σ_I , and turns out to be flexible enough to also account for the distribution of background fluorescence intensities in the transcriptionally inactive states (O_{off} or P_{off}). Indeed, the above distribution captures the empirical distribution of intensities decently well (Fig. S5F), and the specific choice we made here did not impact significantly our state calling.

Next, the transition between the three states (O_{off} , P_{off} , and P_{on}) is defined by the generator or Laplacian matrix of the system according to the network in Fig. S5A:

$$G = \begin{pmatrix} -f_1 & b_1 & b_3 \\ f_1 & -b_1 - f_2 & b_2 \\ 0 & f_2 & -b_2 - b_3 \end{pmatrix}. \quad (\text{S6})$$

The resulting transition probabilities $P(\lambda_t|\lambda_{t-1})$ in Eq. S3 are then computed as the matrix exponential of G , i.e. $P(\lambda_t|\lambda_{t-1}) \equiv \exp[G\Delta t]$, where Δt is the sampling time interval. The initial state distribution $P(\lambda_0)$ is chosen as the steady state distribution of the system, which is obtained by solving the linear system $GP = 0$.

Lastly, Θ represents the entire set of parameters governing the observed distances, the observed intensities, and the state transition rates with a total of six physical scales and five kinetic parameters that need to be inferred:

$$\Theta = \{\sigma_R(O_{\text{off}}), \sigma_R(P_{\text{off}}), \sigma_R(P_{\text{on}}), \sigma_I(O_{\text{off}}), \sigma_I(P_{\text{off}}), \sigma_I(P_{\text{on}}), f_1, f_2, b_1, b_2, b_3\}. \quad (\text{S7})$$

Due to the underlying symmetries of our model, the eleven parameters above are not fully identifiable (structural identifiability). Indeed, in the absence of structure imposed on the σ_R and σ_I , the states O_{off} , P_{off} and P_{on} could be permuted and the inference would be degenerate. However, as we mentioned in the beginning of this section (see Fig. S4), we have some prior knowledge about the structure of the system. From the data, it is clear that $\sigma_R(O_{\text{off}}) \geq \sigma_R(P_{\text{off}}) \simeq \sigma_R(P_{\text{on}})$ and $\sigma_I(O_{\text{off}}) \simeq \sigma_I(P_{\text{off}}) \leq \sigma_I(P_{\text{on}})$ should be satisfied. Thus, to break the symmetries, we decided to enforce $\sigma_R(P_{\text{off}}) = \sigma_R(P_{\text{on}}) \equiv \sigma_R(P)$, effectively reducing the number of parameters by one. The same treatment could be performed on the σ_I 's (i.e., enforcing $\sigma_I(O_{\text{off}}) = \sigma_I(P_{\text{off}})$), further reducing the number of parameters. Instead, we decided to keep these three parameters free as a control and monitor the relative scale of the σ_I 's.

Inferring Θ for each clone individually (i.e., for different genomic separation s) is a challenging task, given a large number of parameters (i.e., ten) and the risk of overfitting. This is especially true for the clones for which we have limited data ($n \sim 50$ traces for $s = 57, 82$, and 88 kb, see Table S6). However, given our system, most of the parameters could be shared among the clones since genomic separation is unlikely to affect all the σ_I 's, $\sigma_R(P)$, and the rates $\{f_2, b_1, b_2, b_3\}$ related to the $P_{\text{off}} \leftrightarrow P_{\text{on}}$ transitions and the *homie-homie* unbinding transition $P_{\text{off}} \rightarrow O_{\text{off}}$. To drastically simplify our inference problem, we thus initially made the assumption that only f_1 and $\sigma_R(O_{\text{off}})$ are clone-specific (and thus depend on genomic

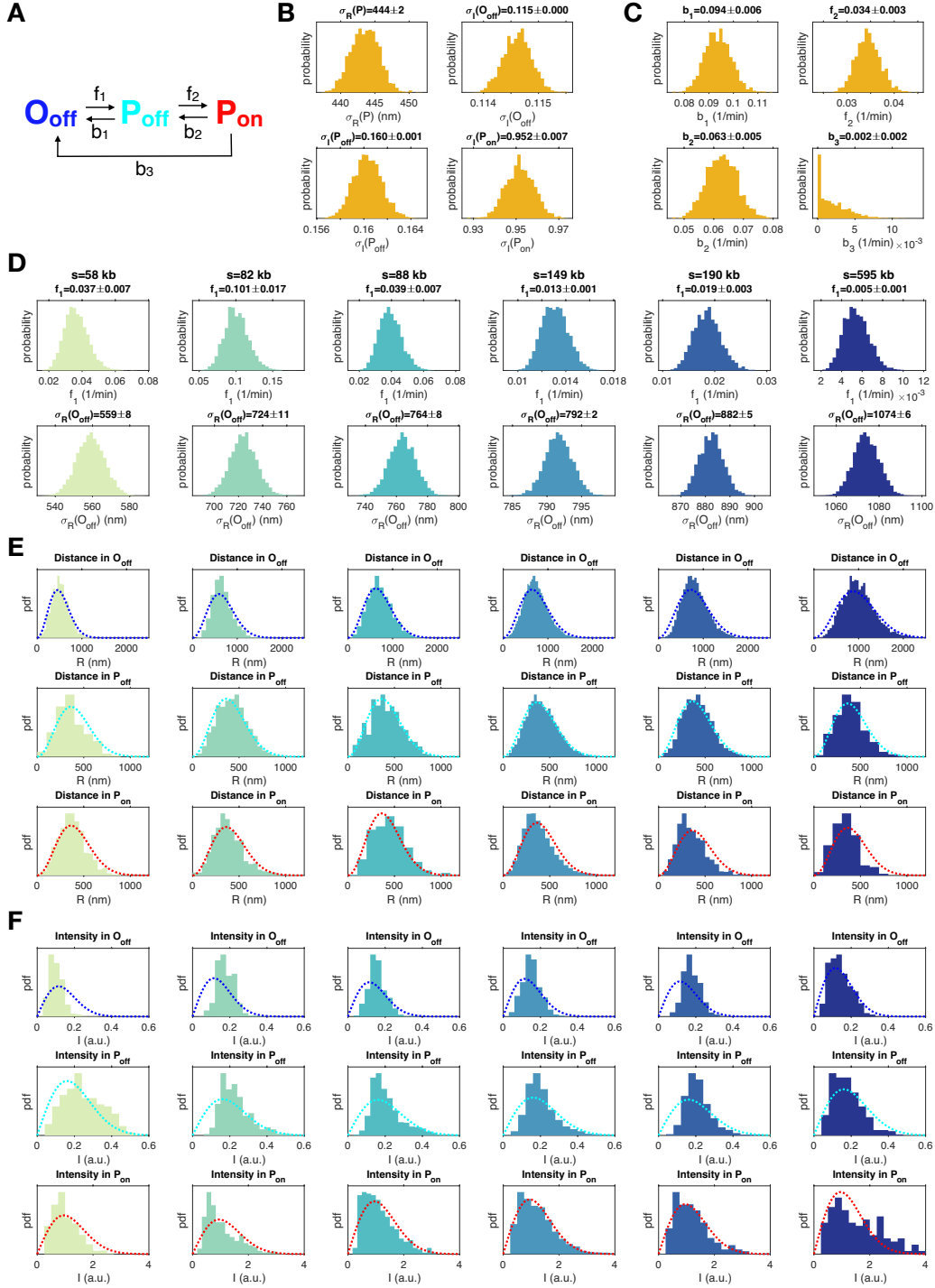


Figure S5: Calibration of a hierarchical HMM model to infer topological and transcriptional states. (A) Schematic of the latent state transitions learned. (B) Posterior distributions $P(\Theta|D)$ of the global parameters $\Theta = \{\sigma_R(P), \sigma_I(O_{off}), \sigma_I(P_{off}), \sigma_I(P_{on})\}$ related to the observation distributions. (C) Posterior distributions $P(\Theta|D)$ of the transition rates that are shared among the different clones, i.e., parameters that are assumed independent of genomic separation. (D) Posterior distributions $P(\Theta|D)$ of the parameters that are specific to each clone, i.e., the distance $\sigma_R(O_{off})$ and the rate f_1 . (E) Comparison between the calibrated observation distributions (dotted lines, Eq. (S4)) using the inferred $\sigma_R(O_{off})$ and $\sigma_R(P)$ and the underlying state based empirical distributions for distances. (F) Comparison between the calibrated observation distributions (dotted lines, Eq. (S5)) using the inferred $\sigma_I(O_{off}), \sigma_I(P_{off})$ and $\sigma_I(P_{on})$ and the underlying state based empirical distributions for intensities.

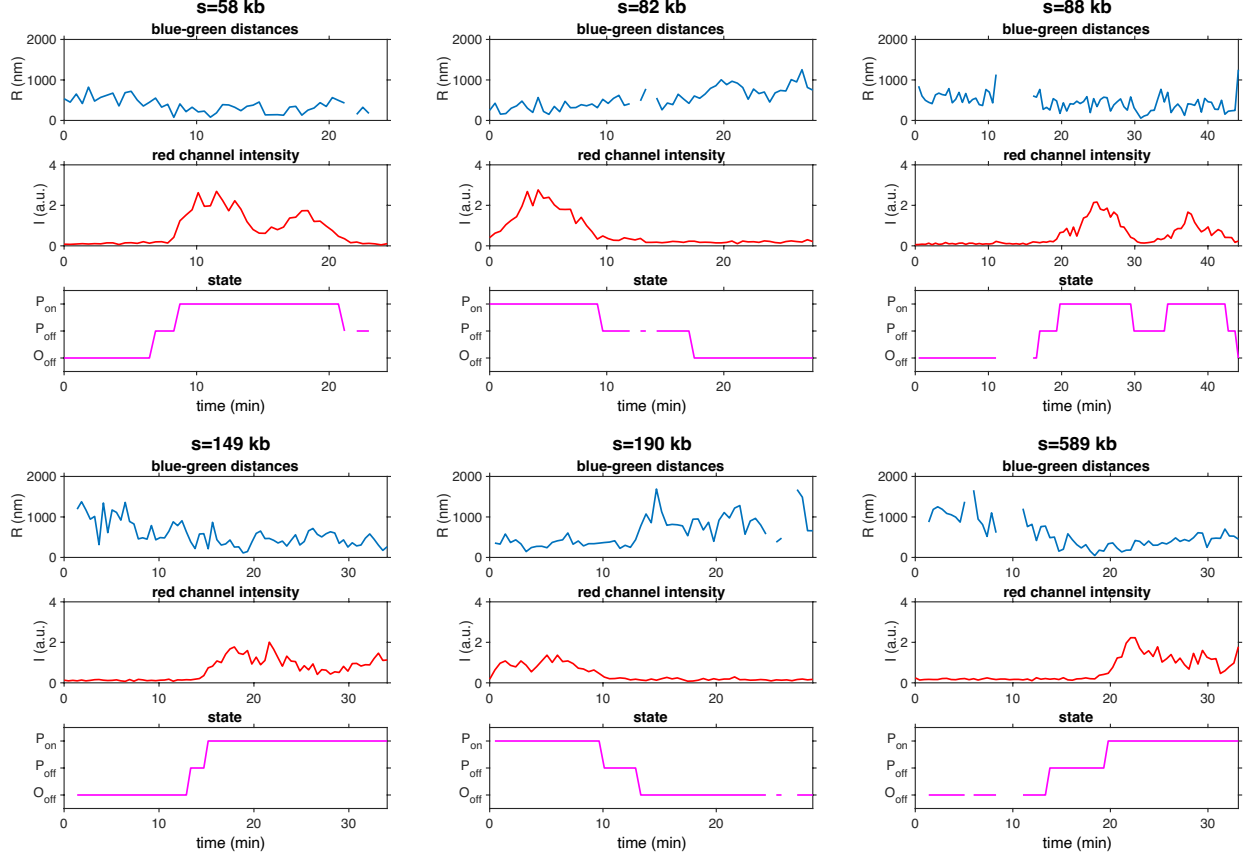


Figure S6: **Example trajectories for various genomic separations.** For each genomic separation s , one input pair of blue-green distance R and red transcriptional fluorescence intensity I are shown on top of the inferred state. The inferred state is obtained as the argmax of the posterior decoding $P(\lambda_t|D)$ computed using the calibrated hierarchical HMM (see Fig. S5).

separation s), whereas all the other parameters are shared among the clones. Such a structure defines a hierarchical model characterized by the following likelihood function:

$$P(\mathcal{D}|\Theta_H) = \prod_{j=1}^{N_s} P(\mathcal{D}(s_j)|\Theta = \{\Theta_G, \Theta_j\}), \quad (\text{S8})$$

where $\mathcal{D} = \{\mathcal{D}(s_1), \dots, \mathcal{D}(s_{N_s})\}$ is the full data set made of all the genomic separation s_j , $P(\mathcal{D}(s_j)|\Theta)$ is the likelihood of the data for a specific s_j (see Eq. S2), $\Theta_H = \{\Theta_G, \Theta_1, \dots, \Theta_{N_s}\}$ is the ensemble of parameters, among which $\Theta_G = \{\sigma_R(P), \sigma_I(O_{\text{off}}), \sigma_I(P_{\text{off}}), \sigma_I(P_{\text{on}}), f_2, b_1, b_2, b_3\}$ are the global parameters that are shared for all s_j , and $\Theta_j = \{\sigma_R(O_{\text{off}}), f_1\}$ are the local parameters specific to each s_j . Notably, this assumed hierarchical structure leads to a massive reduction in the number of parameters, namely $\#\Theta = 8 + 2 \cdot N_s$ instead of $\#\Theta = 10 \cdot N_s$ (with $N_s = 6$, $\#\Theta = 20$ versus $\#\Theta = 60$ respectively).

We first estimated the joint posterior distribution $P(\Theta_H|\mathcal{D})$ of our hierarchical model (S8). The posterior $P(\Theta_H|\mathcal{D})$ was sampled using an MCMC sampler [79], which enables estimation of the marginal posterior distribution for each parameter. All the marginal posterior distributions are shown in Fig. S5B-D, and the resulting parameter estimates (mean and standard deviation) can be found in Table S2 and S3. Interestingly, the posterior of the rate b_3 looks like the prior (log-uniform), and the mean rate b_3 is much smaller than b_2 . This clearly indicates that the contribution of b_3 to the model dynamics is negligible and

$\sigma_R(P)$ (nm)	$\sigma_I(O_{\text{off}})$ (a.u.)	$\sigma_I(P_{\text{off}})$ (a.u.)	$\sigma_I(P_{\text{on}})$ (a.u.)
444 ± 2	0.115 ± 0.000	0.160 ± 0.001	0.952 ± 0.007
b_1 (1/min)	f_2 (1/min)	b_2 (1/min)	b_3 (1/min)
0.094 ± 0.006	0.034 ± 0.003	0.063 ± 0.005	0.002 ± 0.002

Table S2: Global parameters Θ_G of the hierarchical HMM model estimated using MCMC.

s (kb)	$\sigma_R(O_{\text{off}})$ (nm)	f_1 (1/min)
58	559 ± 8	0.037 ± 0.007
82	724 ± 11	0.101 ± 0.017
88	764 ± 8	0.039 ± 0.007
149	792 ± 2	0.013 ± 0.001
190	882 ± 5	0.019 ± 0.003
595	1074 ± 6	0.005 ± 0.001

Table S3: Local parameters Θ_j of the hierarchical HMM model estimated using MCMC.

b_3 can safely be considered to be zero. Moreover, we found that $\sigma_I(O_{\text{off}}) \simeq \sigma_I(P_{\text{off}}) < \sigma_I(P_{\text{on}})$ as expected.

Leveraging the inferred parameters of the hierarchical model, we then reconstructed the states underlying the inter-locus distance and transcriptional activity of individual nuclei using a Viterbi algorithm and posterior decoding [78]. These algorithms take as input the time series of the distances R and red fluorescence values I of a single nucleus. The Viterbi algorithm finds a single state trajectory $\Lambda = (\lambda_0, \lambda_1, \dots)$ that maximizes $P(\Lambda | \mathcal{D}_i, \Theta)$, namely the most likely trajectory given the data and the inferred parameters. Alternatively, we also used posterior decoding that enables computation of the state marginal distribution $P(\lambda_t | \mathcal{D}_i, \Theta)$ at time t given the data and the inferred parameters. A single state trajectory $\Lambda = (\lambda_0, \lambda_1, \dots)$ can then be computed from the state marginal distribution as $\lambda_t = \text{argmax} P(\lambda_t | \mathcal{D}_i, \Theta)$. It turns out that for our system, both approaches, either the Viterbi or Posterior decoding, predict essentially the same underlying latent state trajectories (see example in Fig. 2C,D and Fig. S6). The overall state reconstruction statistics using the hierarchical model are given in Table S4.

Using the state inference, we then checked whether the emission probabilities $P(R|\lambda)$ and $P(I|\lambda)$ (Eq. S4 and S5) calibrated with the inferred parameters $\{\sigma_R(O_{\text{off}}), \sigma_R(P)\}$ and $\{\sigma_I(O_{\text{off}}), \sigma_I(P_{\text{off}}), \sigma_I(P_{\text{on}})\}$

s (kb)	N_{nuclei}	$N(O_{\text{off}})$	$N(P_{\text{off}})$	$N(P_{\text{on}})$
58	55	36	24	28
82	59	43	56	23
88	58	47	35	15
149	579	555	203	73
190	166	144	65	26
595	164	161	21	4

Table S4: State statistics based on the hierarchical HMM. Total number of measured nuclei (N_{nuclei}) and number of nuclei for which at least one given state ($N(O_{\text{off}})$, $N(P_{\text{off}})$ and $N(P_{\text{on}})$) is observed as a function of the genomic distance s .

s (kb)	$\sigma_R(O_{\text{off}})$ (nm)	$\sigma_R(P)$ (nm)	f_1 (1/min)	b_1 (1/min)	f_2 (1/min)	b_2 (1/min)
58	560 ± 7	404 ± 6	0.023 ± 0.007	0.079 ± 0.023	0.110 ± 0.026	0.063 ± 0.014
82	738 ± 13	464 ± 5	0.089 ± 0.019	0.058 ± 0.011	0.032 ± 0.006	0.098 ± 0.019
88	770 ± 8	476 ± 7	0.044 ± 0.009	0.099 ± 0.020	0.035 ± 0.009	0.075 ± 0.021
149	793 ± 2	440 ± 3	0.014 ± 0.001	0.098 ± 0.008	0.029 ± 0.003	0.066 ± 0.007
190	876 ± 5	420 ± 6	0.014 ± 0.003	0.089 ± 0.016	0.036 ± 0.008	0.046 ± 0.009
595	1071 ± 6	378 ± 10	0.005 ± 0.001	0.124 ± 0.032	0.020 ± 0.011	0.050 ± 0.025

Table S5: HMM parameters Θ estimated separately for each genomic separation s using MCMC.

match the empirical distribution (Fig. S5E,F). Overall, the agreement is excellent supporting the validity of our inference. Lastly, to test our assumption behind our hierarchical model, that most parameters are shared, we perform inference for each genomic separation separately. To do so, we fixed $\sigma_I(O_{\text{off}})$, $\sigma_I(P_{\text{off}})$ and $\sigma_I(P_{\text{on}})$ to the values of the calibrated hierarchical model (Table S2) and we set $b_3 = 0$ as this parameter appeared unnecessary (see paragraph above). We then re-estimated $f_1, f_2, b_1, b_2, \sigma_R(O_{\text{off}})$ and $\sigma_R(O_P)$ for each clone individually and these can be found in Table S5. Overall, the resulting parameter values are very close to the estimates of the hierarchical model (see also section 2.5, and Fig. S10), thus supporting our key assumption.

2.2 Validating the HMM using simulated data

To validate our reconstruction of the states and the inference of the underlying transition rates, we tested our HMM approach on simulated data. We aimed to generate synthetic data sets that mimic real data, namely simulated data that satisfy the same latent state transition with realistic rates $\{f_1, b_1, f_2, b_2, b_3\}$ and observation parameters $\{\sigma_R(O_{\text{off}}), \sigma_R(P), \sigma_I(O_{\text{off}}), \sigma_I(P_{\text{off}}), \sigma_I(P_{\text{on}})\}$ (Fig. S5).

We chose to test our approach on three different genomic separations; short ($s = 58$ kb), medium ($s = 149$ kb), and long ($s = 595$ kb). For each s , we generated 300 time-series of blue-green distance R and transcriptional intensity I , whose duration equaled 40 min and sampling time $\Delta t \simeq 30$ s as in real data. Time series for the blue-green distance were generated using simulations of a Rouse polymer model with 1000 beads. We tracked the position of two beads equidistant from the central bead of the polymer, with a separation $s/2$ from the center such that the "genomic distance" was given by $s = 58, 149, 595$ beads. We then rescaled time and length scales such that the relaxation time of the polymer $\tau = s^2$ and the average inter-locus distance matched the experimental values for each value of s . To capture the dependence of the transition from the O_{off} to the P_{off} state on the dynamics of the 3D distance, we defined a simple implementation of distance-dependent *homie-homie* binding. Specifically, we defined a success rate of *homie-homie* binding r , such that the two ends of the polymer bind with probability r when in close proximity (defined by a threshold on the 3D distance of 400 nm). The parameter r was assumed constant for all simulations and set to 0.1% to approximately reproduce the f_1 rate estimated from real data. Note that this parameter r cannot be compared to the biological success rate of real *homie* binding, as it depends on the time scale at which the system is sampled. Once the two *homie* elements are bound, we include an additional linear spring linking the two loci, with spring constant $k_{\text{link}} = 0.02k$, where $k = 1$ is the spring constant of the backbone of the polymer. The parameter k_{link} was chosen to generate distances R whose mean $\langle R \rangle \simeq 400$ nm in the P_{off} and P_{on} state. In addition, once the P_{off} state is reached, we ran a Gillespie algorithm to simulate the transition from the P_{off} to P_{on}

state and from the P_{off} back to the O_{off} state [80]. The Gillespie simulation was performed according to the state transition in Fig. S5A, with rates set by the global parameters determined from real data (Table S2 and $b_3 = 0$).

Next, to simulate the intensities I in the O_{off} and P_{off} state (i.e., the background), we generate uncorrelated samples from a Rayleigh distribution with parameter $\sigma_I(O_{\text{off}})$ and $\sigma_I(P_{\text{off}})$ set from Table S2, respectively. Lastly, to simulate the transcriptional intensities in the P_{on} state, we sampled in log space from a Gaussian process $\tilde{I}(t)$ with mean $\tilde{\mu}$, variance $\tilde{\sigma}^2$ and covariance function $K(t, t')$. We chose $K(t, t') = \exp(-|t - t'|/\tau_e)$ (Ornstein–Uhlenbeck) and we set the correlation time to $\tau_e = 2$ min, which approximates the temporal correlation in the transcriptional signal. The mean $\tilde{\mu}$ and the variance $\tilde{\sigma}^2$ were defined such that the intensity time-series in real-space $I(t) = \exp(\tilde{I}(t))$ is log-normal distributed with mean and variance equal to a Rayleigh distribution of parameter $\sigma_I(P_{\text{on}})$ determined from Table S2. Namely, $\tilde{\mu}$ and $\tilde{\sigma}^2$ are given by:

$$\tilde{\mu} = \log\left(\frac{\pi\sigma_I(P_{\text{on}})}{2\sqrt{2}}\right) \quad \text{and} \quad \tilde{\sigma}^2 = \log\left(1 + \frac{4 - \pi}{\pi}\right) \quad (\text{S9})$$

All the simulated time series were assumed to start in the O_{off} state. As an example, a pair of simulated distance R and intensity I time series is shown in Fig. S7C.

With these three simulated data sets in hand (i.e., with $s = 58, 149,$ and 595 kb), we can compare the inferred to the input parameters that were used to generate the simulated data. We performed the HMM inference for each data set separately, by sampling the joint posterior distribution $P(\Theta|\mathcal{D})$ with MCMC as described in section 2.1. Thus, for each data set, we estimated the ten free parameters all at once, namely $\Theta = \{\sigma_R(O_{\text{off}}), \sigma_R(P), \sigma_I(O_{\text{off}}), \sigma_I(P_{\text{off}}), \sigma_I(P_{\text{on}}), f_1, f_2, b_1, b_2, b_3\}$. The resulting marginal posterior distributions for $s = 149$ kb are displayed in Fig. S7A with the input (true) parameters highlighted by a vertical dashed line. For each simulated data set, we estimated the relative error on all parameters. Overall, the absolute relative error for the rates is 30% on average (Fig. S7B top), while for the observation parameters, these are 7% on average (Fig. S7B bottom). Thus, even when estimating all the parameters at once (hardest case), the errors remain reasonable and clearly allow us to distinguish different scales among the parameters.

Having checked our ability to infer parameters correctly, we next tested whether our state inference is accurate. We thus performed posterior decoding using our trained HMM on the three simulated data sets, as described in section 2.1. The whole state reconstruction for $s = 149$ kb is shown in Fig. S7D,E; the inferred state trajectories are visually hardly distinguishable from the ground truth. Assessing our reconstruction error on all simulated data sets, we recovered the correct state for more than 95% of the time points (Fig. S7F). Overall, the state inference is excellent and does not strongly depend on the underlying error on the rate parameters, since the signatures of the different states in the data are rather strong (especially for O_{off} and P_{on}).

2.3 Single trajectory state analysis

Here, we demonstrate that the majority of single-cell trajectories explore the full range of interlocus distances that are sampled by the whole ensemble of trajectories in all three inferred states. From the ensemble of state trajectories (Fig. S8A), we plot the distance distributions for every single trajectory as a function of its inferred transcriptional and topological state (Fig. S8B-C). We find that in the majority

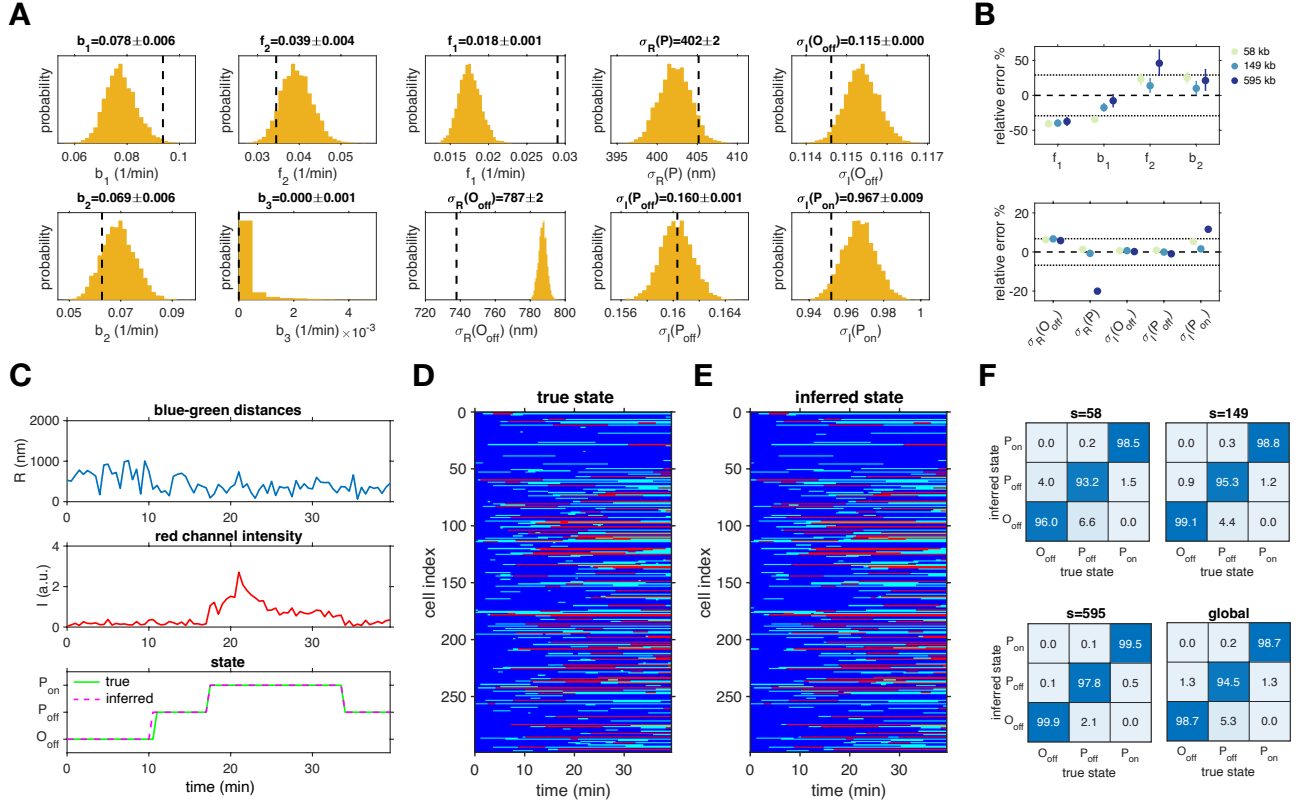


Figure S7: **Validating the HMM inference on simulated data.** (A) Posterior distributions $P(\Theta|D)$ estimated using simulated data with genomic separation $s = 149\text{kb}$. Vertical dashed lines indicate the input parameters used for generating the data. (B) Relative error (in %) with respect to input values on the inferred rates (top) and distances (bottom) for three simulated data sets with different genomic separation (color code; $s = 58, 149$ and 595kb). (C) State inference on simulated data. (D) True states for the entire simulated data set $s = 149\text{kb}$. (E) Inferred states for the entire simulated data set $s = 149\text{kb}$. (F) Fraction of inferred states as a function of true input (in %) for all simulated data sets.

of cases, the single trajectory distributions approximately match the population-averaged distribution, suggesting that the single-cell trajectories explore the full range of distances of each state.

As a more stringent criterion, we perform a hypothesis test of the null hypothesis that the single-cell distribution is indistinguishable from the ensemble-averaged distribution. Specifically, we use the two-sided Kolmogorov-Smirnov test comparing for each trajectory the single-trajectory distribution to the population distribution. The null hypothesis that the distributions are the same is rejected if $p < 0.05$. We find that for most data sets, for the majority of trajectories in all states for all genomic separations, the null hypothesis is not rejected (Fig. S8E).

2.4 Estimation of transcriptional lifetime

To estimate the lifetime of transcriptional activity, we use the inferred state trajectories (section 2.1) to calculate the typical time the system remains in the P_{on} state. Lifetime estimation is challenging due to the problem of censoring, referring to the fact that trajectories may start or end in the P_{on} state, which gives only partial access to the lifetime in such a trajectory. To deal with this problem, we use the Kaplan-Meier estimator for the survival function of the transcription lifetimes [81]. The survival function $S(t)$ gives the probability that the transcriptionally active state has *not* transitioned to a transcriptionally

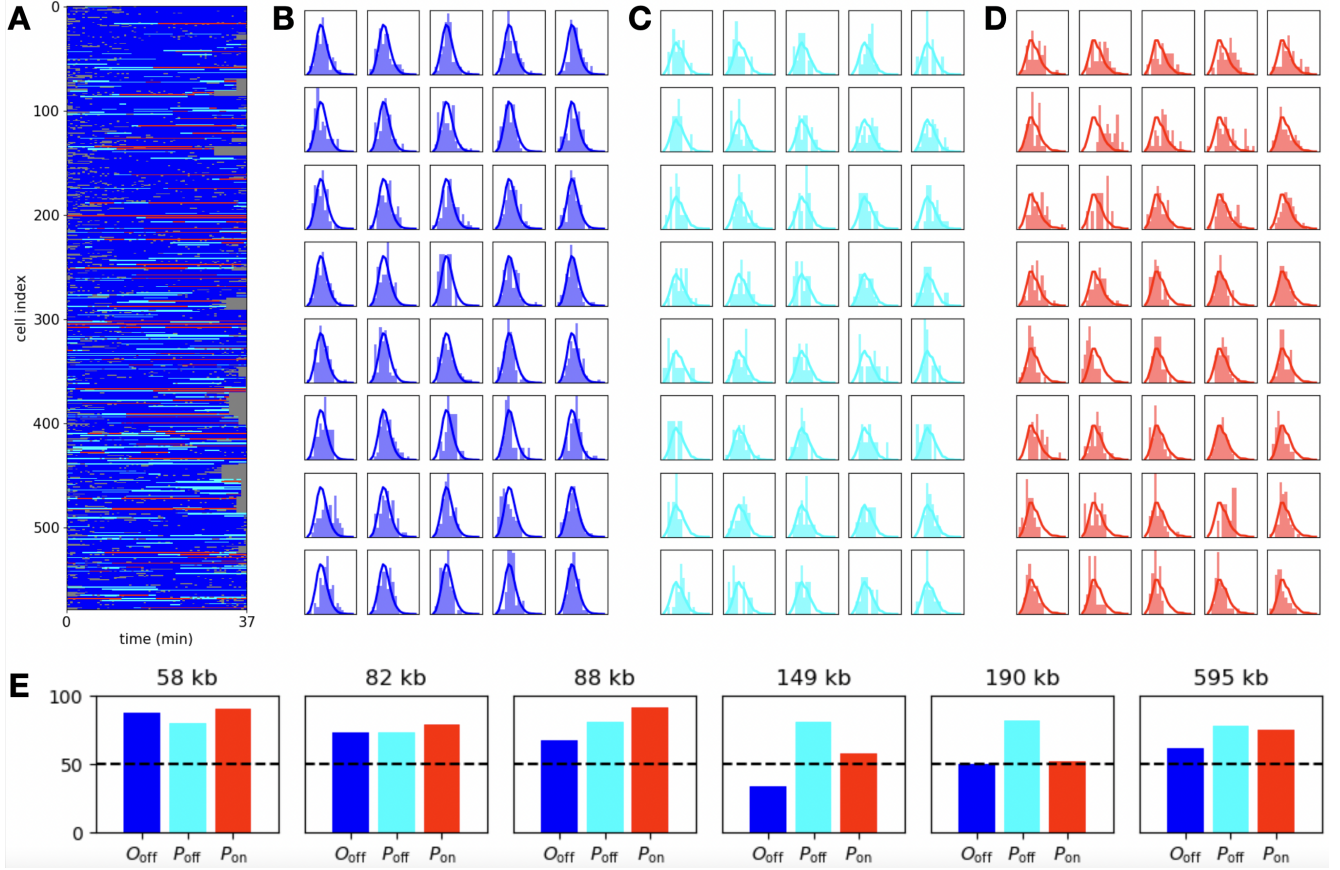


Figure S8: **Single-trajectory interlocus distance distributions.** (A) All state trajectories for genomic separation $s = 149$ kb. (B-D) Single trajectory interlocus distance distributions for the three states ($s = 149$ kb). Each panel shows the distance distribution of a single trajectory as a bar histogram and the population-averaged distribution as a solid line. Only trajectories with at least ten time points are included to ensure sufficient statistics for comparison. (E) Percentage of trajectories for which the null hypothesis that the single-cell and the population distribution are the same is not rejected, for each state and genomic separation.

inactive state, and is defined as

$$S(t) = 1 - \int_0^t p(t') dt' \quad (\text{S10})$$

where $p(t)$ is the probability distribution of transcriptional lifetimes. We use the Kaplan-Meier estimator [26,81]

$$\hat{S}(t) = \prod_{t_i < t} \left(1 - \frac{N_{\text{uncensored}}^{(i)}}{N^{(i)}} \right) \quad (\text{S11})$$

where $N_{\text{uncensored}}^{(i)}$ is the number of uncensored events of length t_i and $N^{(i)}$ is the number of events with length larger than t_i . From this estimator, we obtain the survival curves shown in the main text Fig. 2C and Fig. S9A. From these curves, the estimate of the median lifetime can be determined by finding the intercept where $\hat{S}(\text{median}[\tau_{\text{trans}}]) = 0.5$.

A second method to estimate the median lifetime is a maximum likelihood estimate under the assumption that the lifetime distribution is exponential, i.e.

$$p(t) = \frac{1}{\langle \tau_{\text{trans}} \rangle} e^{-t/\langle \tau_{\text{trans}} \rangle} \quad (\text{S12})$$

where $\langle \tau_{\text{trans}} \rangle$ is the mean transcriptional lifetime. Then, the maximum likelihood estimate of $\langle \tau_{\text{trans}} \rangle$ is given by [26]

$$\widehat{\langle \tau_{\text{trans}} \rangle} = \frac{1}{N_{\text{uncensored}}} \sum_i t_i \quad (\text{S13})$$

and the median lifetime is given by $\ln(2) \widehat{\langle \tau_{\text{trans}} \rangle}$.

The median lifetime estimates from both methods are given in main text Fig. 2D. For the genomic separation of 595 kb, there are only 5 observed P_{on} states out of a total of 164 trajectories, meaning that the lifetime is hard to estimate for this sample (see last panel of Fig. S9A). For 3.3 Mb, there are no observed P_{on} states.

Furthermore, we compare these estimates to simply taking the mean of all observed lifetimes (Fig. S9B), showing that also in this case, there is no variation with genomic separation, and the typical lifetime is ≈ 10 min.

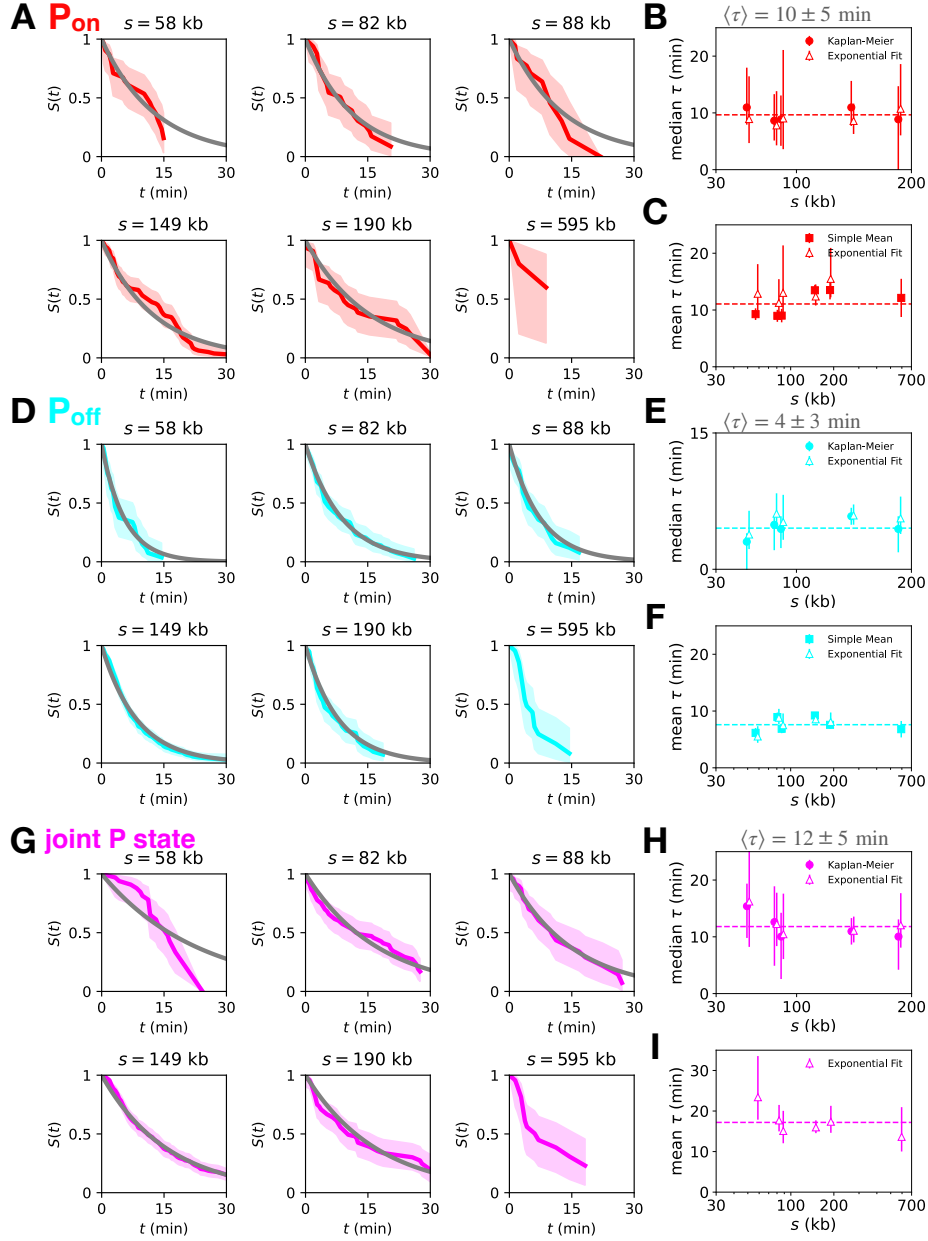


Figure S9: **Lifetime-estimation using survival probability curves.** (A) Kaplan-Meier survival curves for each genomic separation. Shaded regions: 95% confidence intervals [26]. Grey lines: exponential fits obtained by using the maximum likelihood mean lifetime (using Eq (S13) in Eq. (S12)). (B) Median lifetimes obtained by the exponential fit (triangles), or by reading off the time at which the Kaplan-Meier survival curves cross $S = 0.5$ (dots). Equivalent to main text Fig. 2D for the P_{on} state. The mean of median lifetimes across genomic separations is noted above (error bars: standard deviation calculated from total variance). (C) Mean lifetimes obtained by the exponential fit (triangles) and by simply taking the mean of all observed lifetimes (squares). Errorbars on exponential fit results represent 95% confidence intervals [26], and on means represent bootstrap error bars. Panels A-C are for the P_{on} state (red), while panels D-F show the same plots for the P_{off} state (cyan), and panels G-I for the joined paired state when the system is either in P_{on} or P_{off} (magenta).

2.5 HMM parameter scaling analysis

To assess which parameters of our HMM model scale with genomic separation s , we systematically compare the parameters of our global inference using the hierarchical model to the parameters obtained by doing inference on each s separately (see also section 2.1). The hierarchical model was built on the

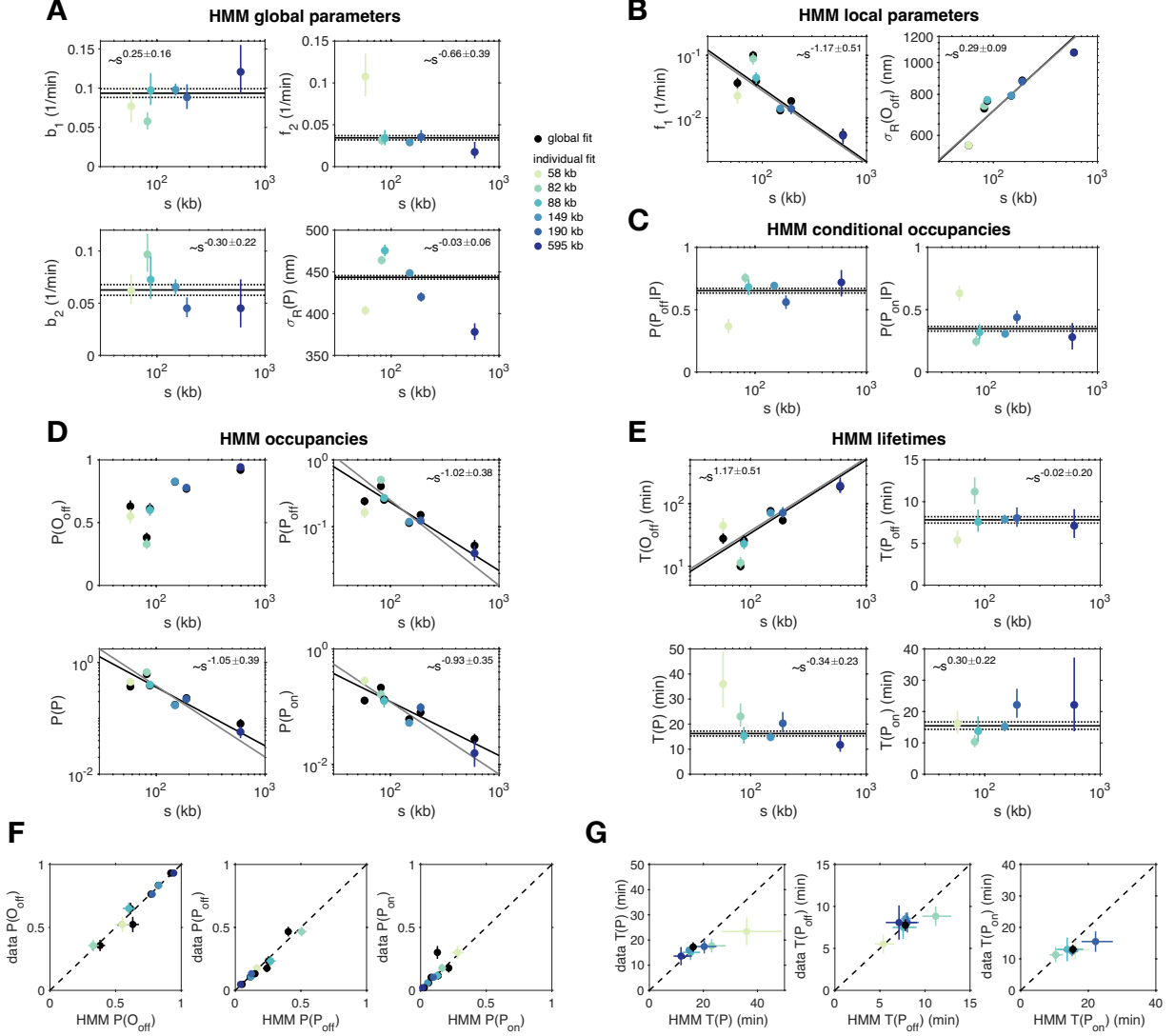


Figure S10: **Scaling of the HMM parameters, the predicted state-occupancy and state-lifetime.** **A,B**, Inferred parameters as a function of genomic separation s . **(A)** These parameters were assumed shared among the clones in the hierarchical model. Performing the inference separately for each individual clone leads to the parameter values that remain close to the ones obtained using the hierarchical model (black solid and dashed line, mean and standard deviation respectively). **(B)** These parameters were assumed to scale with genomic separation s . Performing the inference separately for each individual clone preserves the scaling observe with the hierarchical model (gray line, power-law fit). **(C)** HMM-predicted conditional occupancy of P_{off} and P_{on} states as a function of genomic separation s . **(D)** HMM-predicted occupancy of the different states as a function of genomic separation s . **(E)** HMM-predicted residence time within the different states as a function of genomic separation s . **(F)** Comparison between HMM-predicted and measured occupancies. **(G)** Comparison between HMM-predicted and measured lifetimes.

assumption that most parameters are independent of s , and thus can be shared across clones (Eq. S8).

We first analyzed the parameters that were assumed to not scale with s (Fig. S10A), namely the distance $\sigma_R(P)$ and the rates $\{f_2, b_1, b_2\}$ related to the $P_{\text{off}} \leftrightarrow P_{\text{on}}$ transitions and the *homie-homie* unbinding transition $P_{\text{off}} \rightarrow O_{\text{off}}$. Overall, these parameters, when inferred separately for each s , remain numerically very close to the global estimate (black line) made with the hierarchical model. In addition, the power-law exponents characterizing the scaling of these parameters as a function of s are close to zero (within error bars), validating our assumption that these are mostly independent of s . Next, we investigated the parameters that were assumed to scale with s (Fig. S10B), namely the open distance $\sigma_R(O_{\text{off}})$ and

the rate f_1 . When these parameters are inferred separately for each s , we again recover values that are numerically very close to the global estimate (black dots). The observed scaling of the parameters with s is very similar between the two inference approaches (hierarchical vs individual model, black and gray lines respectively). Moreover, the estimated scaling exponents are significantly different from zero and match the estimation based on data (Fig. 2).

Next, we investigated the impact of the parameter scaling on the steady-state occupancy (i.e., the probability) of the three states. To calculate the occupancy, we solved analytically the steady state equation $GP = 0$, where G is the Laplacian matrix of the system (Eq. S6). We obtained the following expression for the probabilities as a function of the rates:

$$P(O_{\text{off}}) = \frac{b_1 b_3 + b_1 b_2 + f_2 b_3}{Z} \quad (\text{S14})$$

$$P(P_{\text{off}}) = \frac{(b_3 + b_2) f_1}{Z} \quad (\text{S15})$$

$$P(P_{\text{on}}) = \frac{f_2 f_1}{Z} \quad (\text{S16})$$

$$Z = b_1 b_3 + b_1 b_2 + f_2 b_3 + (b_3 + b_2 + f_2) f_1. \quad (\text{S17})$$

Using the equations above, the conditional probabilities $P(P_{\text{off}}|P)$ and $P(P_{\text{on}}|P)$ are easily calculated:

$$P(P_{\text{off}}|P) = \frac{b_3 + b_2}{f_2 + b_3 + b_2} \quad (\text{S18})$$

$$P(P_{\text{on}}|P) = \frac{f_2}{f_2 + b_3 + b_2} \quad (\text{S19})$$

$$(\text{S20})$$

Interestingly, both $P(P_{\text{off}}|P)$ and $P(P_{\text{on}}|P)$ do not depend on f_1 , and thus are not expected to vary with genomic separation s . Indeed, when computing these conditional probabilities using the parameters of the hierarchical model (Fig. S10C, black line), we found $P(P_{\text{off}}|P) = 0.65$ and $P(P_{\text{on}}|P) = 0.35$, which are independent on s and match the values estimated from data Fig. 2E. Similarly, when computing these probabilities using the parameters from the individual fits (Fig. S10C, color dots), the probabilities cluster around the global estimate (albeit $s = 58$ kb appears to be an outlier).

We then investigated the scaling of the occupancies themselves (Eq. S14). Given our parameter regime, we expect the following scaling for the probabilities: $P(O_{\text{off}}) \sim 1/(c + f_1)$ and $P(P) \sim P(P_{\text{off}}) \sim P(P_{\text{on}}) \sim f_1$, where $f_1 \sim s^{-1.17 \pm 0.51}$ (see Fig. S10B). We computed these probabilities using both the hierarchical and individual fit parameters and found scaling relationships that are very consistent with our expectation (Fig. S10D).

Next, we investigated the scaling of the lifetime (mean residence time) of the different states. In our HMM framework, the lifetimes are phase-type distributed and are easily computed from the state tran-

sition matrix (Eq. S6). We found:

$$T(O_{\text{off}}) = \frac{1}{f_1} \quad (\text{S21})$$

$$T(P_{\text{off}}) = \frac{1}{b_1 + f_2} \quad (\text{S22})$$

$$T(P_{\text{on}}) = \frac{1}{b_2 + b_3} \quad (\text{S23})$$

$$T(P) = \frac{f_2 + b_2 + b_3}{b_1 b_2 + b_1 b_3 + f_2 b_3} \quad (\text{S24})$$

Only $T(O_{\text{off}})$ depends on f_1 , and thus varies with s , whereas $T(P_{\text{off}})$, $T(P_{\text{on}})$ and $T(P)$ are supposed to be mostly independent on s . We computed these lifetimes using both the hierarchical and individual fit parameters and found scaling relationships that are again very consistent with our expectation (Fig. S10E). Indeed, $T(P_{\text{off}})$, $T(P_{\text{on}})$ and $T(P)$ are essentially constant, while $T(O_{\text{off}})$ varies as the inverse of f_1 .

Lastly, we compared the occupancies and lifetimes predicted by the HMM parameters to the occupancies and lifetimes estimated from data based on state splitting (Fig. S10F,G). Overall, the excellent agreement between the different quantities predicted by the HMM parameters and the ones estimated from data (using state splitting) supports the validity of our inference and is indicative of the mathematical consistency of our approach. Importantly, it should be noted that such an agreement is not necessarily trivial. Indeed, the HMM model mainly acts as a prior for the state inference, thus if the data possessed features that could not be accounted for by the model, discrepancies would have arisen.

2.6 Results without state splitting

The analysis of the two-locus dynamics shown in the main text is done for the O_{off} only. To demonstrate that our results on the two-locus dynamics do not sensitively depend on the details of the state inference, we compare the statistics of the O_{off} state to those obtained from the entire data set comprising all three states. Since the data are dominated by the O_{off} state, the state splitting does not have a strong impact on most statistics, especially for large genomic separations. As expected, the average distances of the full data are lower than those of the O_{off} state only, and the inferred two-locus diffusion coefficients Γ_2 are lower. However, key scaling exponents are not strongly affected, including the scaling of the inferred relaxation times τ (Fig. S11).

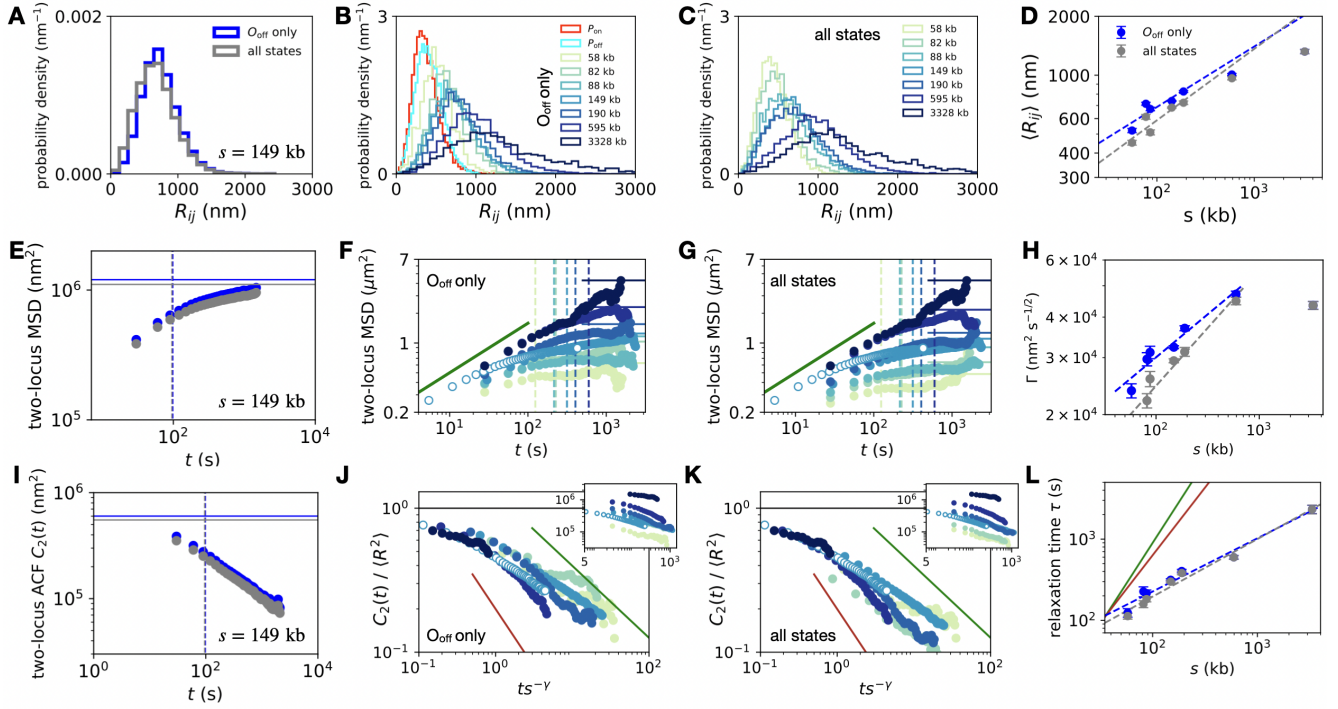


Figure S11: **Two-locus analysis is independent of state inference.** (A) Probability distributions of the inter-locus distances R_{ij} ($s = 149$ kb). Blue: distribution for the O_{off} state only, as shown in main text Fig. 2A. Grey: distribution for all states. (B,C) Probability distributions of the inter-locus distances R_{ij} for all separations, with (B) and without state splitting (C). (D) Scaling of mean inter-locus distance with (blue) and without state splitting (grey). (E,F,G) Two-locus MSD $M_2(t)$, with inferred values of the relaxation time τ (dashed lines) and the asymptote $2\langle R^2 \rangle$. (H) Scaling of the two-locus diffusion coefficient with genomic separation with (blue) and without state splitting (grey). (I,J,K) Two-locus ACF $C_2(t)$, with inferred values of the relaxation time τ (dashed lines) and the asymptote $2\langle R^2 \rangle$. (L) Scaling of the inferred relaxation time with genomic separation with (blue) and without state splitting (grey).

2.7 Analysis of no-homie data

To test the role of the *homie* insulator-mediated focal contacts for the transcriptional dynamics in our system, we employ a reporter construct in which the *homie* sequence is replaced by a λ DNA sequence of the same length. In this system, only two topological states are possible: a transcriptionally inactive configuration O_{off} and a transcriptionally active configuration P_{on} . To account for this in our state inference, we simplified our HMM hierarchical model by only modeling the $O_{\text{off}} \leftrightarrow P_{\text{on}}$ transitions with rates f_1 and b_1 . Thus, we had only four global parameters $\{\sigma_R(P_{\text{on}}), \sigma_I(O_{\text{off}}P_{\text{on}}), \sigma_I(P_{\text{on}}), b_1\}$ and two local parameters $\{\sigma_R(O_{\text{off}}), f_1\}$ to infer from the no-*homie* data. The resulting inferred parameters are displayed in Fig. S12. The state inference was then performed using this model specifically calibrated on the no-*homie* data.

Based on the state trajectories, we find that there is still frequent transcriptional activity for genomic separation 58 kb ($8.5 \pm 0.8\%$), but almost none ($< 1\%$ of time-points) for 149 kb (Fig. S13A). We furthermore compare the statistics of the 3D inter-locus distance between the *homie* and no-*homie* constructs of the same genomic separation. Due to the different statistics of the state dynamics in the two constructs, we compare data from the O_{off} state in both cases. We find that distance distributions largely overlap (Fig. S13B). The two-locus MSDs also exhibit a similar shape and are well fitted by the ideal chain theoretical expression, although we observe small, but not systematic, differences in the two-locus diffusion coefficient between *homie* and no-*homie* constructs (Fig. S13C).

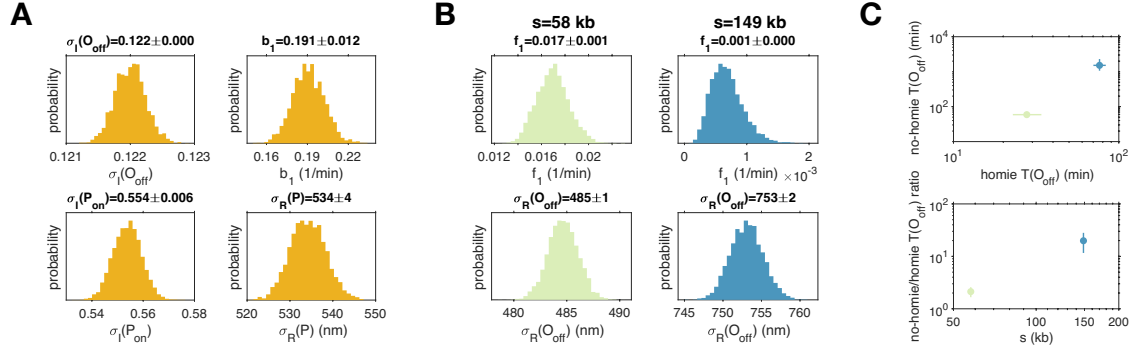


Figure S12: **Calibration of the hierarchical HMM model for the no-homie data.** (A) Posterior distributions of the global parameters $P(\Theta|D)$ estimated using the no-homie data with genomic separation $s = 58$ kb and $s = 149$ kb. (B) Posterior distributions $P(\Theta|D)$ of the clone specific-parameters, which vary with genomic separation s . (C) Comparison of the HMM-predicted open state lifetime $T(O_{\text{off}})$ between the homie and no-homie data.

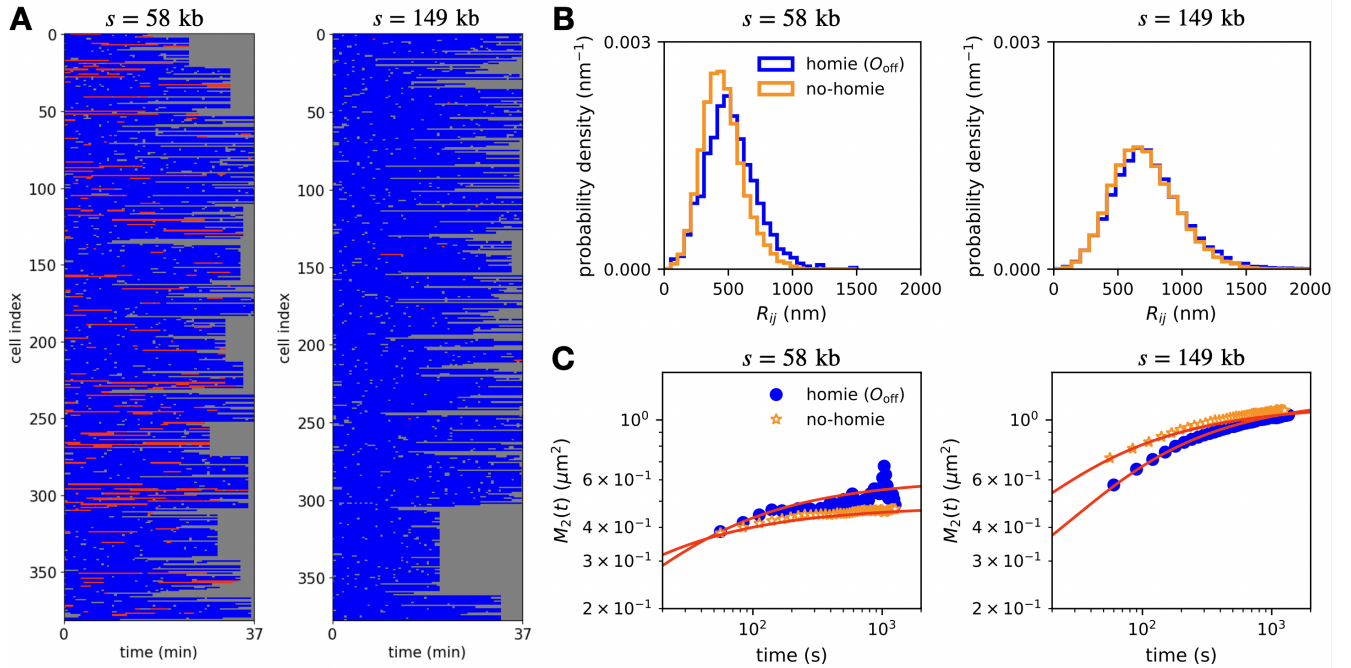


Figure S13: **The open state dynamics is not affected by the presence of homie.** (A) All state trajectories for no-homie constructs with genomic separations 58 and 149 kb. (B) Probability distributions of the inter-locus distances R_{ij} . Blue: distribution for the O_{off} state of homie constructs, orange: distributions of the transcriptionally inactive state in no-homie constructs. (C) Two-locus MSD $M_2(t)$ with Rouse fits shown as red lines.

3 Analysis of single-locus dynamics

The analysis of the motion of single chromosomal loci is only possible if any displacement and rotation of the cell nucleus as a whole is corrected for, as this would affect the apparent dynamics of the DNA loci. This problem does not affect relative measures based on the inter-locus distance vector $\mathbf{R}_{ij}(t)$ (section 4.1). In particular, correcting rotations is challenging as at least three loci need to be tracked to infer global rotations. Previous works have therefore focused solely on the statistics of the inter-locus distance [26, 35, 41], or, in recent work, relied on multi-locus tracking to correct global movement [27].

In our system, however, the only global mode to be corrected is an overall affine translation of the cell nuclei within the embryo, which we can correct by nucleus tracking in the xy -directions (section 1.3). Nucleus tracking is difficult in the axial z -direction. Therefore, we estimate the statistics of single locus diffusion using the xy -components of the dynamics.

To characterize the motion of single loci, we calculate the single-locus mean-square-displacement (MSD) defined in each spatial dimension $i = \{x, y, z\}$ as

$$M_1^{(i)}(t) = \left\langle |r_i(t_0 + t) - r_i(t_0)|^2 \right\rangle_{t_0} = \Gamma_1^{(i)} t^\beta \quad (\text{S25})$$

where averages are averages over time and samples. The 3D MSD is then given by $M_1(t) = M_1^{(x)}(t) + M_1^{(y)}(t) + M_1^{(z)}(t)$. Assuming that all three spatial dimensions are identical, we estimate $M_1(t)$ from the x and y components via $M_1(t) = \frac{3}{2}(M_1^{(x)}(t) + M_1^{(y)}(t))$.

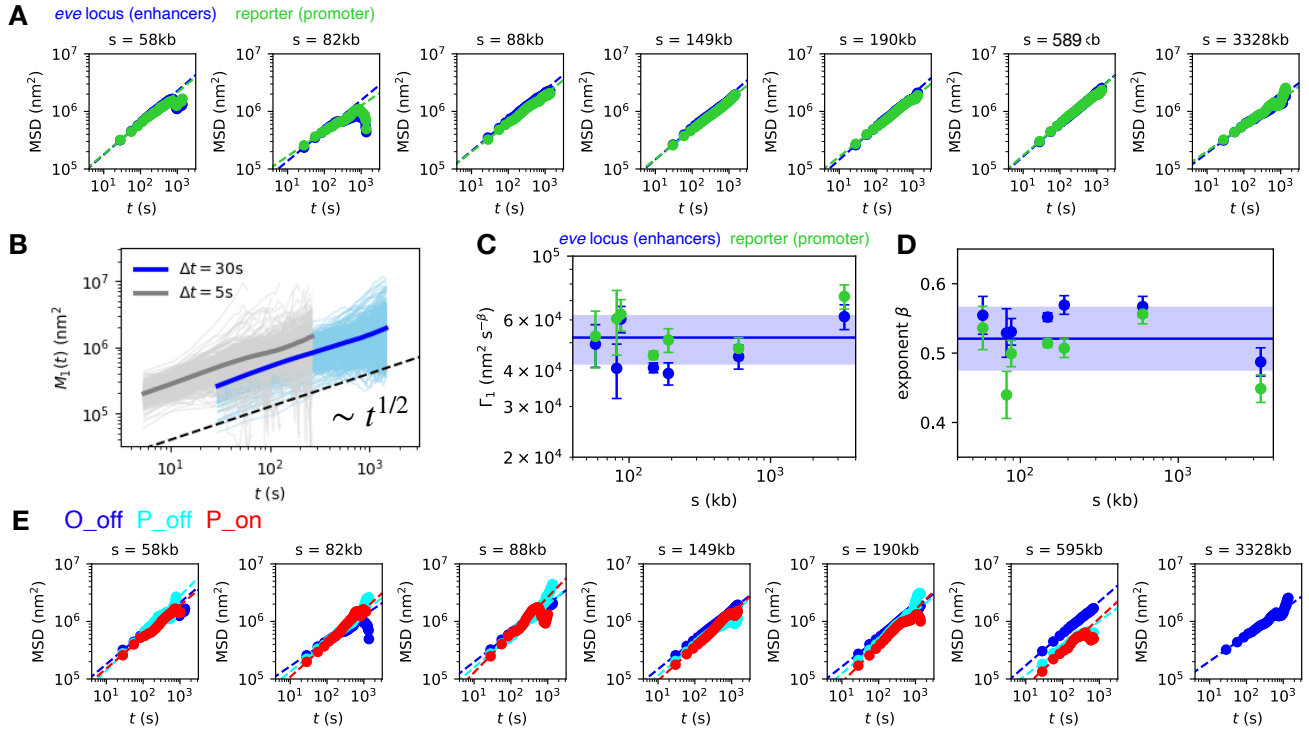


Figure S14: **Analysis of single-locus dynamics.** (A) Single-locus MSDs $M_1(t)$ for the enhancer (blue) and promoter (green) for each genomic separation s , estimated from xy -components of the trajectories. Dashed lines indicate linear fits to the first 5 data points. (B) Single-locus MSDs $M_1(t)$ for $s = 149$ kb at two different imaging time-intervals $\Delta t = 5$ s (grey) and $\Delta t = 30$ s (blue). Thin lines indicate the MSDs of single trajectories. (C) Single-locus diffusion coefficients Γ_1 measured using the linear fits in panel (A). (D) Single-locus diffusion exponents β measured using the linear fits in panel (A). (E) Single-locus MSDs $M_1(t)$ for the three topological states O_{off} (blue), P_{off} (cyan), P_{on} (red) for each genomic separation s . Dashed lines indicate linear fits to the first 5 data points. All MSDs are given in nm^2 .

We find that the single-locus MSD is consistent across enhancer vs promoter loci, for different genomic separations, for different imaging time intervals, and for the three inferred topological states (Fig. S14).

Additionally, we also report the velocity autocorrelation functions of single loci [34], given by

$$C_v(t) = \langle \mathbf{v}^{(\delta)}(t_0) \cdot \mathbf{v}^{(\delta)}(t_0 + t) \rangle_{t_0} \quad (\text{S26})$$

where velocities are calculated over variable time-interval $\delta = n\Delta t$ where Δt is the imaging time-interval: $\mathbf{v}^{(\delta)}(t) = (\mathbf{r}(t + \delta) - \mathbf{r}(t))/\delta$. We find that these correlations collapse with δ and are well

described by the Rouse model prediction [34,55] (Fig. S15):

$$\frac{C_v^{(\delta)}(t)}{C_v^{(\delta)}(0)} = \frac{|t - \delta|^\beta + |t + \delta|^\beta - 2|t|^\beta}{2\delta^\beta} \quad (\text{S27})$$

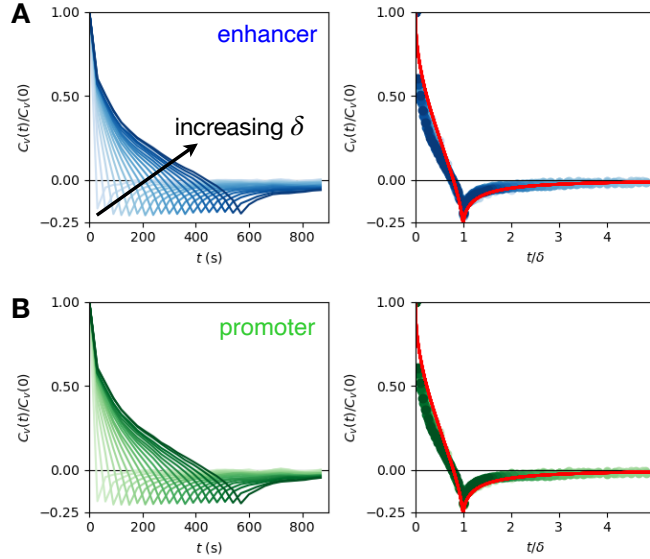


Figure S15: **Velocity autocorrelation functions** $C_v(t)$. (A) Left: $C_v^{(\delta)}(t)/C_v^{(\delta)}(0)$ as a function of t with increasing δ for enhancer motion. Right: $C_v^{(\delta)}(t)/C_v^{(\delta)}(0)$ as a function of t/δ , showing that the functions collapse. Red line: Theory prediction for the Rouse model (Eq. (S27)) with $\beta = 1/2$. Curves shown here are for $s = 149$ kb. Similar results are obtained for all other genomic separations. (B) Same as (A) for promoter motion.

4 Analysis of two-locus dynamics

In this section, we provide details of how we test the theoretical predictions from section 5 using experimental data by calculation of two-locus MSDs, inference of the relaxation time (section 4.1) and collapsing the two-locus autocorrelations (section 4.2). Note before any further analysis, we correct \mathbf{R}_{ij} to account for chromatic aberration (section 1.4).

4.1 Two-locus MSD and relaxation time inference

The observed scaling of the single-locus MSD with an exponent close to 1/2 suggests as well as the long-time scaling of the two-locus autocorrelation, which is close to the ideal chain exponent suggests that we may fit the two-locus MSD with the analytical prediction obtained for the ideal chain Rouse model [26]. We use the expression for an infinite continuous polymer; for discussion of the assumption $s \ll N$, see section 5:

$$M_2(t) = 2\Gamma_2 t^{1/2}(1 - e^{-\tau/\pi t}) + 2J \operatorname{erfc}[(\tau/\pi t)^{1/2}] \quad (\text{S28})$$

where $J = \langle R^2 \rangle$ and $\tau = (J/\Gamma_2)^2$. Note that we refer to the diffusion coefficient obtained from the two-locus MSD as Γ_2 , while we write Γ_1 for the single locus diffusion coefficient. For the ideal or crumpled chain models, $\Gamma_1 = \Gamma_2$. However, we do not make this constraint on the data *a priori*.

To explicitly test the assumed Rouse-like scaling of the diffusive part of the two-locus MSD, we examine the exponent of the early-time subdiffusive regime ($t \ll \tau$). At the shorter genomic separations, our data with $\Delta t = 30$ s does not sample the regime $t \ll \tau$ (Fig. S16A,B). Therefore, we focus on data sets that contain at least five data points in the regime $t < \tau$ and fit the exponent β , which we find to be close to the single-locus estimates and consistent with $\beta = 1/2$ (Fig. S16C).

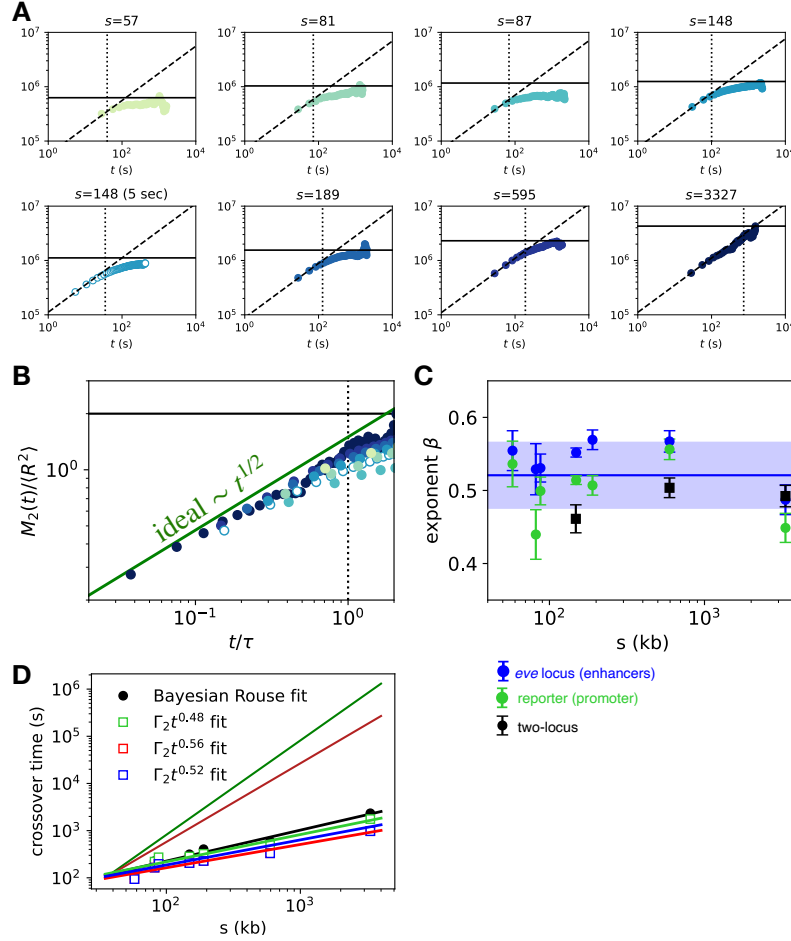


Figure S16: **Subdiffusive exponents of the two-locus MSD and relaxation time estimation with simple intercept fitting.** (A) Two-locus MSDs $M_2(t)$ for each genomic separation. Solid lines show the value of $2\langle R^2 \rangle$. Dashed lines are fits of $2\Gamma_2 t^{0.5}$. Dotted lines show the intercept of the fit with $2\langle R^2 \rangle$, providing an estimate for the relaxation time τ for each of the two scenarios. (B) All two-locus MSD curves collapsed by normalizing time by the relaxation time and the MSD by the typical squared distance $\langle R^2 \rangle$. The points in the regime $t \ll \tau$ show scaling close to the ideal chain exponent of $1/2$. (C) Subdiffusive exponents measured from two-locus MSDs for those data sets with at least five data points in the regime $t < \tau$ ($s = 148$ kb, $\Delta t = 5$ s; $s = 595$ kb; $s = 3.3$ Mb) (black data points), compared to results from the single locus MSDs (blue and green data points). (D) Estimated cross-over times from both the Bayesian inference of the full Rouse dependence used in the main text (Eq. (S28), black filled dots) and linear log-fits with the measured experimental dynamic exponent $\beta = 0.52$ (blue open squares), our lower ($\beta = 0.52 - 0.04 = 0.48$; green) and upper bound ($\beta = 0.52 + 0.04 = 0.56$; red) of the dynamic exponent.

We find that the two-locus MSDs are well-fitted by Eq. S28, and the fitted value of J coincides with the measured asymptote $\langle R^2 \rangle$ (Fig. S17A). Additionally, the presence of measurement errors in the tracking affects the MSD curves, leading to an additive contribution of $4(\sigma_x^2 + \sigma_y^2 + \sigma_z^2)$, reflecting that the error can be different in each spatial direction. We perform a Bayesian maximum likelihood fit of the two-locus MSD using the python-library tracklib [26] with free parameters $\{J, \Gamma_2, \sigma_z\}$. We use a log-uniform prior for these parameters since they are real, positive, and have some unknown scale. We do not fit measurement errors in the x and y -directions as the estimates for these errors obtained from such a 5-parameter fit are consistent with $\sigma_x = \sigma_y = 0$, and therefore not significant.

To determine the inference errors on the fitted parameters, we perform bootstrapping as described in refs. [82, 83]. Briefly, from each data set of N cell trajectories $\{\mathbf{r}_k\}$, where $k = 1 \dots N$, we generate N_{BS} bootstrap realizations by randomly sampling N trajectories with a replacement for each realization. To obtain the error in the parameters $\{J, \Gamma_2, \sigma_z\}$, we infer their value for each bootstrap realization by performing Bayesian MSD fitting on each realization and take the standard deviation of all obtained fit parameters as our estimate for the error in each fit parameter. The distributions of the bootstrap estimates are shown in (Fig. S17B-D), and range between 1 – 6% in the polymer parameters J, Γ_2 , with larger errors in the inferred measurement error amplitude σ_z .

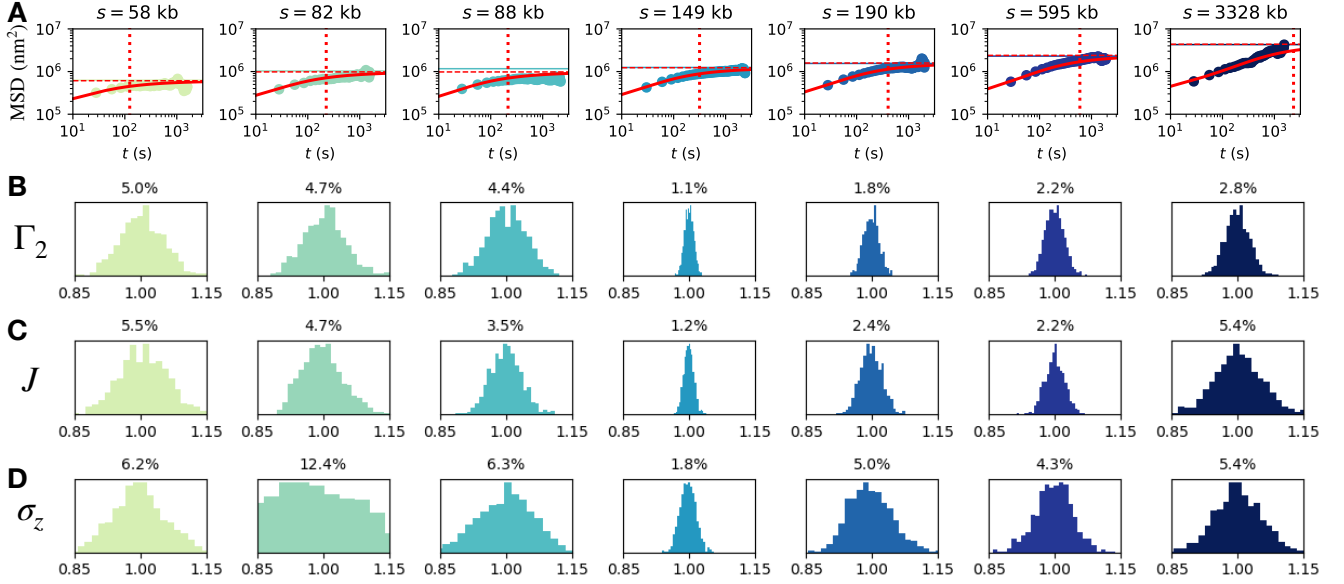


Figure S17: **Two-locus MSD fitting and parameter inference.** (A) Two-locus MSDs $M_2(t)$ for each genomic separation. Solid lines in colors show the value of $2\langle R^2 \rangle$. Solid red lines show the fitted M_2 with measurement error correction. Dashed red lines show the fitted asymptote $2J$ and dotted red lines show inferred relaxation time τ . (B-D) Distributions of the bootstrapped estimates for each parameter, normalised by the maximum a posteriori estimate of each parameter, $\theta/\theta_{\text{MAP}}$.

Furthermore, we demonstrate the accuracy of the relaxation time inference using ideal chain Rouse simulations. Our sampling of the two-locus MSD is limited by two key factors: the imaging time interval Δt and the maximum trajectory length t_{max} . We aim to infer the relaxation time scaling from a set of genomic separations with minimum and maximum relaxation times τ_{min} and τ_{max} , corresponding to the shortest and longest genomic separation. The inference will be limited if $\Delta t > \tau_{\text{min}}$ or $t_{\text{max}} < \tau_{\text{max}}$. Based on the inference from experimental data, the shortest and longest genomic separations are close to these thresholds (Fig. S17A). To test the accuracy of the inference in this case, we generate simulated data with $t_{\text{max}}/\tau_{\text{max}} = 1$ (as in the experimental data for $s = 3.3$ Mb) and vary $\Delta t/\tau_{\text{min}}$ (Fig. S18A). Experimentally, we have $\Delta t/\hat{\tau}_{\text{min}} = 0.76$ (for $s = 58$ kb). The larger this ratio, the more difficult the inference. However, we find that the inference performs well for ratios as high as $\Delta t/\tau_{\text{min}} = 3$, and recovers the correct scaling of the relaxation times for various time intervals to relaxation time ratios (Fig. S18B).

An alternative, simplified way to obtain an estimate of the relaxation time is by fitting the early time two-locus MSD and measuring the intercept with the measured value of $2\langle R^2 \rangle$ (Fig. S16A). This intercept is then given by $\tau \sim (\langle R^2 \rangle / \Gamma_2)^{1/\beta}$. In Fig. S16B, we test this simplified approach for a range of assumed β values, based on our measurement of $\beta = 0.52 \pm 0.04$ from the single-locus MSDs. Specifically, we fit using the mean estimate, $\beta = 0.52$, the lower bound $\beta = 0.52 - 0.04 = 0.48$, and the upper bound

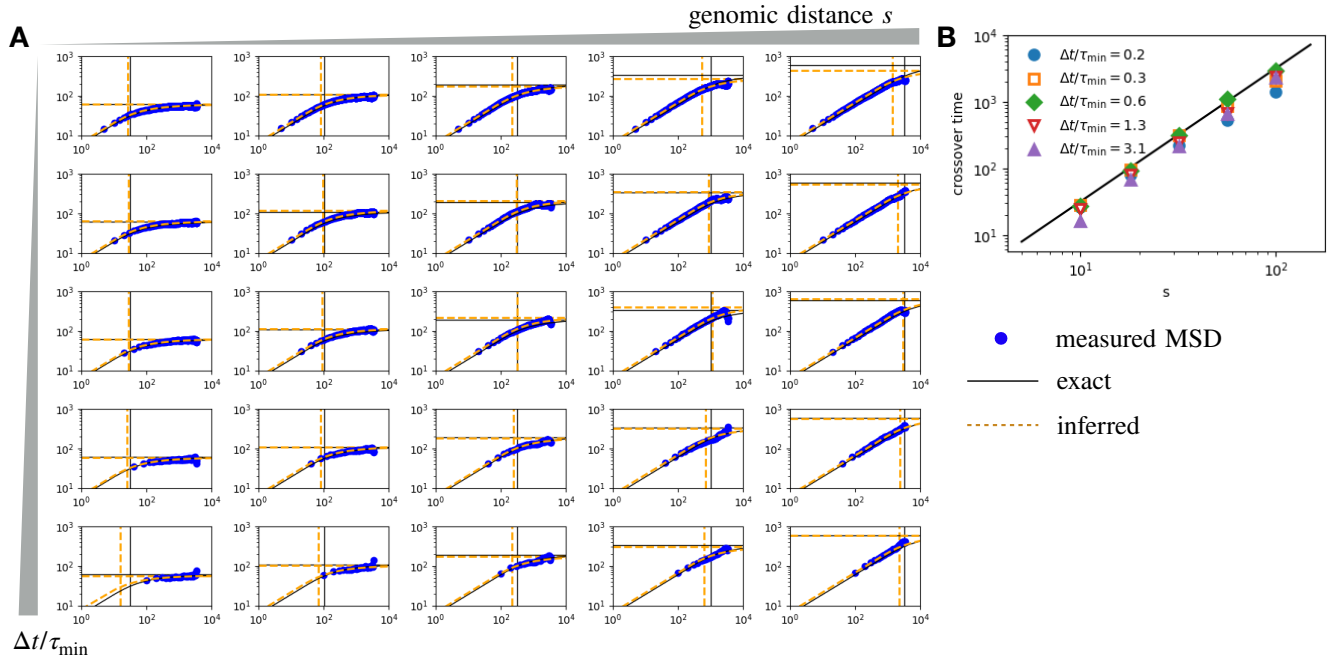


Figure S18: **Testing the relaxation time inference on simulated ideal Rouse chains.** (A) Two-locus MSDs $M_2(t)$. Blue symbols: measured two-locus MSD from the simulations. Black solid lines: exact values of the MSD, the relaxation time, and the plateau $2\langle R^2 \rangle$. Orange dashed lines: inferred values of these three quantities. Horizontal lines show the value of $2\langle R^2 \rangle$, vertical lines show inferred relaxation time τ . Rows correspond to the five tested $\Delta t/\tau_{\min}$ -ratios listed in the legend of panel b. (B) Exact (line) and inferred (symbols) relaxation time scaling for varying $\Delta t/\tau_{\min}$.

$\beta = 0.52 + 0.04 = 0.56$. We find that this simplified approach recovers the strongly reduced scaling exponent compared to the ideal Rouse expectation of $\gamma = 2$ for the full range of dynamic exponents.

Having obtained our estimate for the relaxation times, we compare them to the time scales of transitioning from the O_{off} state to the paired configuration, estimated from the HMM model: $T(O_{\text{off}}) = f_1^{-1}$. We find that these transition times correlate well with the relaxation time (Fig. S19A), and their absolute value is larger by a factor of ten on average (Fig. S19B).

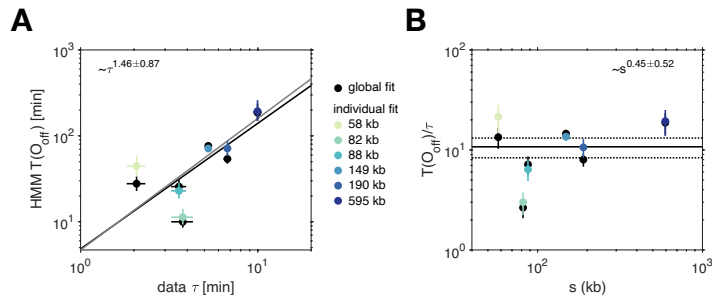


Figure S19: **Open state lifetimes increase with relaxation times.** (A) Lifetime of the open state $T(O_{\text{off}})$ as a function of the polymer relaxation time τ . $T(O_{\text{off}})$ increases with increasing τ . (B) Ratio of the open state lifetime $T(O_{\text{off}})$ and the relaxation time τ as a function of the genomic separation s . The ratio is approximately constant across genomic separation and its value corresponds to a factor 10 on average.

s (kb)	N_{embryos}	N_{nuclei}	$\hat{\sigma}_z$ (nm)	J (nm ²)	Γ_2 (nm ² s ^{-1/2})
58	7	55	200 ± 13	$(2.6 \pm 0.1) \times 10^5$	$(2.4 \pm 0.1) \times 10^4$
82	4	59	177 ± 10	$(4.5 \pm 0.2) \times 10^5$	$(3.0 \pm 0.1) \times 10^4$
88	5	58	210 ± 26	$(4.6 \pm 0.2) \times 10^5$	$(3.1 \pm 0.1) \times 10^4$
149	30	579	204 ± 4	$(5.73 \pm 0.07) \times 10^5$	$(3.23 \pm 0.04) \times 10^4$
190	16	166	220 ± 10	$(7.4 \pm 0.2) \times 10^5$	$(3.70 \pm 0.07) \times 10^4$
595	16	164	213 ± 9	$(1.1 \pm 0.03) \times 10^6$	$(4.7 \pm 0.1) \times 10^4$
3328	10	179	340 ± 10	$(2.1 \pm 0.1) \times 10^6$	$(4.35 \pm 0.09) \times 10^4$

Table S6: **Statistics of the trajectory data sets of all constructs.** From left to right, the columns denote (i) the number of tracked embryos, (ii) the total number of tracked nuclei, (iii) the estimated measurement error in the axial direction, obtained from the MSD fitting, (iv) the fitted value of J , and (v) the fitted value of Γ_2 .

4.2 Two-locus autocorrelation collapse

We make use of the predicted collapse of the two-locus auto-correlation (ACF) (Eq. (S57)) to test the quality of the collapse for the relaxation time exponents for various polymer models and compare them to the anomalous scaling collapse S20. As expected, we find that the correlations do not collapse for the ideal and crumpled chain relaxation time scaling exponents, but they do exhibit an approximate collapse when using the measured relaxation time scaling $\gamma = 0.7$.

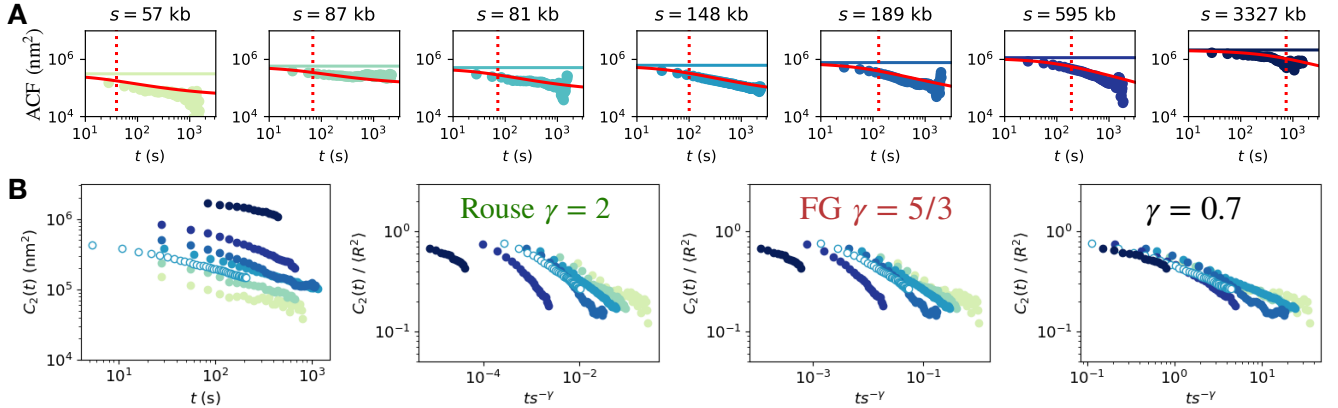


Figure S20: **Two-locus autocorrelation collapse.** (A) Two-locus ACFs $C_2(t)$ for each genomic separation. Solid lines in color: plateau value $2\langle R^2 \rangle$. Red line: ACF expected based on the fitted MSDs, $C_2(t) = (2\langle R^2 \rangle - M_2(t))/2$. (B) All ACFs plotted in absolute units without collapse. (C) ACFs collapsed by the measured value of $\langle R^2 \rangle$ along the y-axis and with the ideal chain relaxation time scaling $\gamma = 2$. (D) Collapse using the crumpled chain relaxation time scaling $\gamma = 5/3$. (E) Collapse using the measured anomalous relaxation time scaling $\gamma = 0.7$.

4.3 Velocity cross-correlations

Error-corrected correlation estimators: To measure the correlations in the joint motion of two loci in absolute motion (within the frame of reference of the cell nucleus), we use the cross-correlations of velocities, defined by

$$C_{vv}^{(\delta)}(t) = \langle \mathbf{v}_i^{(\delta)}(t_0) \cdot \mathbf{v}_j^{(\delta)}(t_0 + t) \rangle_{t_0} \quad (\text{S29})$$

These correlations are challenging to measure as the absolute motion is affected by the global motion of the cell nuclei. Since the syncytial nuclei in the early *Drosophila* embryo are relatively stable and only

exhibit slow affine translations, we correct for global motion in the xy -direction and estimate velocity cross-correlations for the x and y components as done for single locus MSDs (section 3). To further correct the random localization errors in the nucleus tracking, we derive error-corrected correlation estimators. As we show in Fig. S3D, measurement errors in the nucleus tracking are uncorrelated in time. Importantly, however, even time-uncorrelated measurement errors can impact the estimated velocity cross-correlations, because the nucleus movement is subtracted from the motion of both loci, which may lead to spurious additional correlations in their apparent velocities. To overcome this issue, we derive the noise correction terms of the velocity cross-correlations, providing correlation estimators that are unbiased with respect to measurement noise.

Specifically, throughout, we consider the position of locus i in the frame of reference in the nucleus,

$$x_i = r_i - r_n \quad (\text{S30})$$

where r_i is the locus position in the lab frame and r_n is the nucleus position in the lab frame. Our measurement of these positions contains measurement noise, and thus

$$\hat{r}_i = r_i + \sigma_r \eta_i(t) \quad (\text{S31})$$

$$\hat{r}_n = r_n + \sigma_n \xi(t) \quad (\text{S32})$$

where we assume temporally uncorrelated measurement errors, i.e. $\langle \eta_i(t) \rangle = \langle \xi(t) \rangle = 0$ and $\langle \eta_i(t) \eta_j(t') \rangle = \delta_{ij} \delta(t - t')$ and $\langle \xi(t) \xi(t') \rangle = \delta(t - t')$. Here σ_r is the measurement noise in locus tracking and σ_n is the measurement error in the nucleus tracking. Combining these assumptions, we find

$$\hat{r}_i = r_i + \sigma_r \eta_i(t) - \sigma_n \xi(t) \quad (\text{S33})$$

and thus

$$\hat{v}_i^{(\delta)}(t) = (\hat{x}_i(t + \delta) - \hat{x}_i(t)) / \delta \quad (\text{S34})$$

$$= v_i^{(\delta)}(t) + \frac{\sigma_r}{\delta} [\eta_i(t + \delta) - \eta_i(t)] + \frac{\sigma_n}{\delta} [\xi(t + \delta) - \xi(t)] \quad (\text{S35})$$

Multiplying out, we can therefore find the correction terms to various correlation functions. First, we consider the correlation of the locus velocity with the nucleus velocity:

$$\langle \hat{v}_i^{(\delta)}(t) \hat{v}_n^{(\delta)}(0) \rangle = \langle v_i^{(\delta)}(t) v_n^{(\delta)}(0) \rangle + \begin{cases} -2\sigma_n^2 / \delta^2 & t = 0 \\ \sigma_n^2 / \delta^2 & t = \delta \\ 0 & \text{otherwise} \end{cases} \quad (\text{S36})$$

This shows that under the assumption of uncorrelated noise, this correlation should vanish except for $\tau = \{0, \delta\}$, which we verify on the experimental data, validating the assumption of time-uncorrelated tracking errors (Fig. S3D).

Similarly, in the velocity cross-correlations, most terms due to measurement noise average to zero, but the terms due to nucleus tracking errors do not, as the same random error affects both loci:

$$\hat{C}_{vv}(t) = \langle \hat{v}_i^{(\delta)}(t) \hat{v}_j^{(\delta)}(0) \rangle \quad (\text{S37})$$

$$= C_{vv}(t) + \begin{cases} 2\sigma_n^2 / \delta^2 & t = 0 \\ -\sigma_n^2 / \delta^2 & t = \delta \\ 0 & \text{otherwise} \end{cases} \quad (\text{S38})$$

Similarly, for the velocity autocorrelation, we obtain

$$\hat{C}_v(t) = \langle \hat{\delta}_i^{(\delta)}(t) \hat{\delta}_i^{(\delta)}(0) \rangle \quad (\text{S39})$$

$$= C_v(t) + \begin{cases} 2(\sigma_n^2 + \sigma_r^2) / \delta^2 & t = 0 \\ -(\sigma_n^2 + \sigma_r^2) / \delta^2 & t = \delta \\ 0 & \text{otherwise} \end{cases} \quad (\text{S40})$$

Note that the above derivation was done in 1D, for 3D all contributions simply add up, meaning that $\sigma_n^2 \rightarrow \sigma_{n,x}^2 + \sigma_{n,y}^2 + \sigma_{n,z}^2$. Importantly, these corrections show that errors scale with the time-interval δ at which velocities are calculated. Consequently, we find that the estimated velocity cross-correlations are more strongly affected at small δ . To identify how large δ should be for our estimate to be robust against measurement noise, we plot the cross-correlation intercepts $C_{vv}(0)/C_v(0)$ as a function of δ for different values of the estimated measurement error. Based on the fitted measurement errors from the two-locus MSDs (section 4.1), we expect $\sigma \approx 200\mu\text{m}$. We find that for δ in the range of 5 – 60 s, the estimated cross-correlations are strongly affected by realistic measurement error amplitudes (Fig. S21A). In contrast for $\delta > 60$ s, the correlations are largely insensitive to realistic measurement errors for all genomic separations (Fig. S21B). The larger δ , however, the smaller the sample size of available time windows in a finite trajectory, resulting in larger random errors. As a tradeoff, we focus our analysis of velocity cross-correlations on $\delta = 90$ s but additionally show variation with δ in Fig. S22.

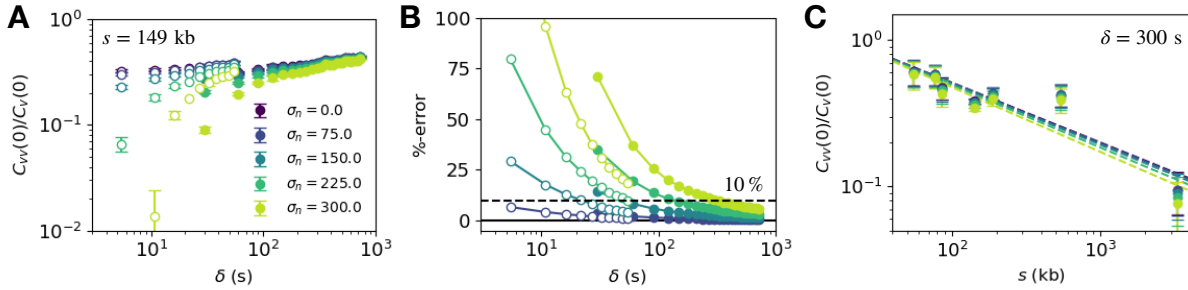


Figure S21: **Error-correction of the velocity cross-correlations.** (A) Normalized velocity cross-correlations as a function of the time-interval δ for $s = 149$ kb. Open symbols: data acquired at imaging rate $\Delta t = 5.4$ s. Closed symbols: data acquired at imaging rate $\Delta t = 30$ s. Different colors correspond to error-corrected correlations assuming different measurement errors (measured in μm), where we take $\sigma_n = \sigma_r = \sigma$. We plot the error-free correlations $C_{vv}(0)/C_v(0)$ calculated from $\hat{C}_{vv}(0)/\hat{C}_v(0)$ according to Eqs. (S37), (S39). (B) Fractional error in the velocity correlations in panel a due to the measurement error contribution, in percent. The dashed line indicates the 10% mark. For $\delta > 90$ s, the errors are $< 10\%$ for all values of σ . Colors as in panel (A). (C) Normalized velocity cross-correlations as a function of the genomic separation s for $\delta = 90$ s. Colors as in (A).

Theory prediction of velocity cross-correlations: The velocity cross-correlation of two loci in the ideal chain Rouse model have been calculated analytically in ref. [55]. Importantly, in the limit $s \ll N$, where N is the total polymer length, and $\delta \ll \tau_N$, where τ_N is the relaxation time of the whole polymer, the cross-correlations of two loci separated by genomic separation s are completely determined by the dimensionless ratio δ/τ , where τ is the relaxation time of the segment s . The correlations are calculated using the tabulated values in ref. [55] (using viscoelastic exponent $\alpha = 1$).

Thus, we can predict the velocity cross-correlations expected based on the inferred relaxation times without any free fitting parameters. We predict the correlations for varying s based on the scaling of relaxation times $\tau = As^\gamma$. First, we predict the expected correlations assuming an ideal chain Rouse scaling of the relaxation time, i.e. $\gamma = 2$. In main text Fig. 4H, we use the prefactor A based on the relaxation time of the shortest genomic separation to the largest genomic separation, i.e. $A_{\text{ideal}}^{(s)} = \tau/s^2$. Here, we additionally demonstrate the ideal chain prediction for varying A , showing that the prediction fails for any possible value of A (Fig. S22A).

To predict the correlations expected based on the anomalous scaling that we find in experiments, we use the measured value of $A = 1.89 \text{ s}\cdot\text{kb}^{-\gamma}$ and $\gamma = 0.7$. Thus, both parameters are fixed based on the experimental data with no additional fitting, giving the blue line in Fig. S22A. Based on the arguments in the previous section, suggesting that larger time intervals δ are less affected by measurement errors, we use $\delta = 300 \text{ s}$ in the main text figure. Here, we additionally show the correlations for varying values of δ (Fig. S22B,D). The functional dependence of the correlations on δ is shown in Fig. S22C. We find that the correlations are generally well predicted by the theory curves that are completely constrained by the inferred relaxation time, with no further fitting involved.

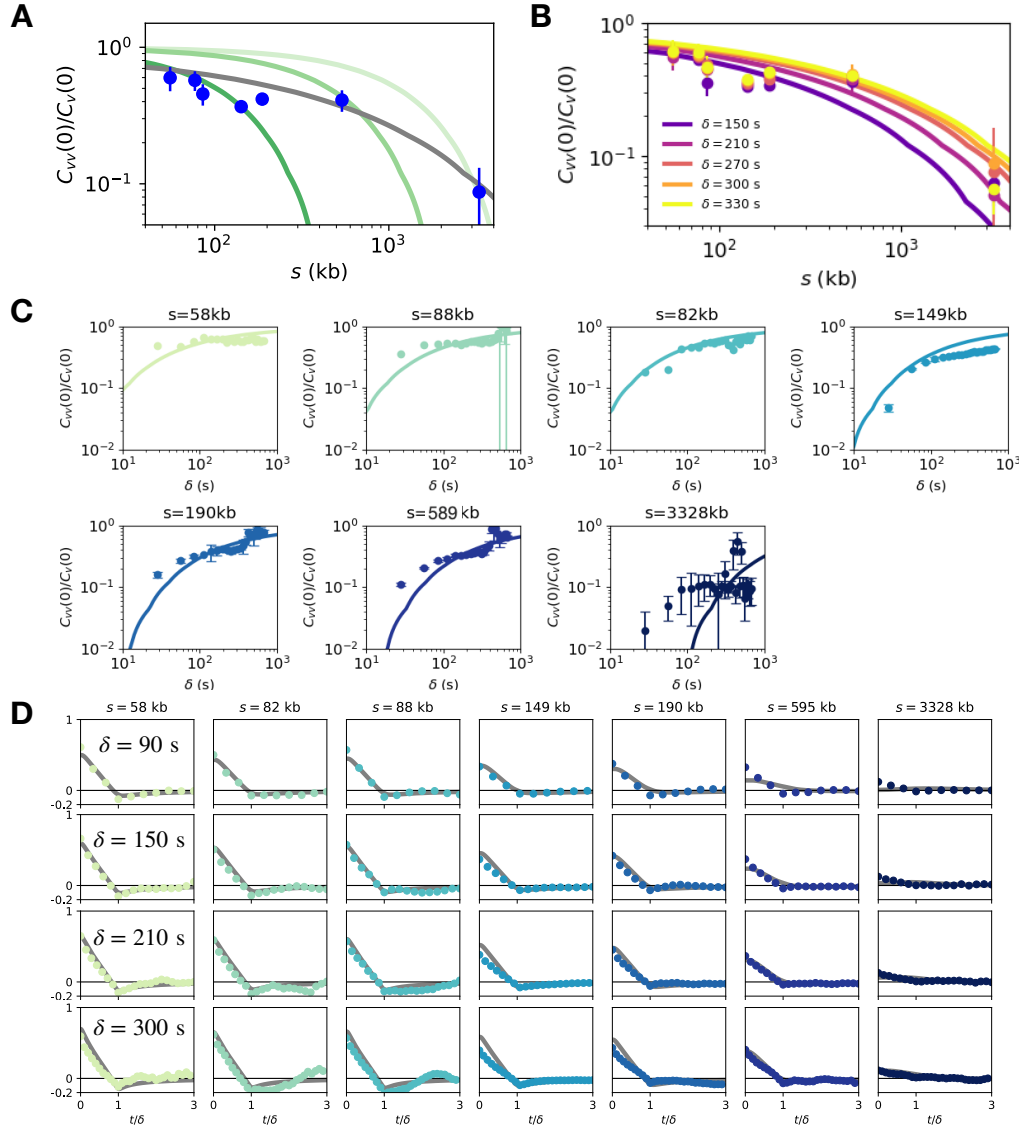


Figure S22: **Theory prediction of velocity cross-correlations.** (A) Comparison of experimental correlations to predictions based on the ideal Rouse scaling $\tau = As^2$, for varying values of A , calculated to match increasing values of $s = \{58 \text{ kb}, 595 \text{ kb}, 3.3 \text{ Mb}\}$, using $A_{\text{ideal}}^{(s)} = \tau/s^2 = \{0.023, 8.1 \times 10^{-4}, 1.01 \times 10^{-4}\} \text{ s}\cdot\text{kb}^{-2}$ (green curves). (B) Anomalous scaling prediction compared to experimental data for various time-intervals δ . (C) Velocity cross-correlations as a function of the time-interval δ (colors), as predicted by the anomalous relaxation time scaling (solid lines) compared to experiments (symbols) (D) Velocity cross-correlation functions $C_{vv}(t)/C_v(0)$ as a function of t/δ for varying δ for each genomic separation. All error bars correspond to bootstrap errors.

5 Two-locus dynamics: theory

In this section, we provide a synthesis of the literature on the scaling exponents measured in this paper and explain the theoretical arguments underlying our analysis and interpretation of two-locus dynamics.

Two-locus MSD: Here, we provide details of how we quantify the joint dynamics of two coupled DNA loci using the two-locus MSD:

$$M_2(t) = \left\langle \left| \mathbf{R}_{ij}(t_0 + t) - \mathbf{R}_{ij}(t_0) \right|^2 \right\rangle_{t_0} \quad (\text{S41})$$

i.e. the MSD of the 3D interlocus distance vector $\mathbf{R}_{ij}(t) = \mathbf{r}_1(t) - \mathbf{r}_2(t)$, where $\mathbf{r}_{1,2}$ are the 3D positions of the two loci.

The two-locus MSD gives insight into the coupled dynamics of the two loci, with two simple limits: at small times $t \ll \tau$, we expect the two-locus MSD to simply reflect the independent diffusion of the two loci, while at large times $t \gg \tau$, the MSD approaches a plateau given by the equilibrium size of the chain. Here, τ is the relaxation time which quantifies the cross-over between the two regimes.

In the large-time regime, the chain segment connecting the two loci has fully relaxed (under the assumption that the system reaches a steady state), meaning that the two-locus MSD is given by the equilibrated size of the chain

$$M_2(t \rightarrow \infty) \rightarrow 2\langle R^2 \rangle \quad (\text{S42})$$

where $\langle R^2 \rangle = \langle |\mathbf{R}_{ij}|^2 \rangle$. For a fractal polymer chain configuration, the average 3D RMS-distance $\sqrt{\langle R^2 \rangle}$ scales with the genomic separation s :

$$\sqrt{\langle R^2 \rangle} \sim s^\nu \quad (\text{S43})$$

where the *static* exponent $\nu = 1/d$ is determined by the fractal dimension d of the polymer. The fractal dimension is $d = 2$ for an ideal chain polymer and $d = 3$ for a crumpled chain.

In the small-time regime, the chain segment connecting the two loci has not had sufficient time to relax, and hence the two loci move independently, meaning that the two-locus MSD is given by the sum of the single-locus MSDs:

$$M_2(t \ll \tau) \approx 2M_1(t) = 2\Gamma t^\beta \quad (\text{S44})$$

Importantly, the dynamic exponent β can be related to the static exponent ν , and thus the fractal dimension d under specific assumptions for the dynamics of the polymer, which we detail below. To avoid confusion, we try to be specific about which assumptions relate to the statics and which to the dynamics. For statics, we use the terms "ideal" and "crumpled chain statistics" for fractal dimensions $d = 2$ and $d = 3$, respectively. For the dynamics of such ideal or crumpled chains, we use the term "generalized Rouse assumption" to refer to the assumption of independent viscous friction on each monomer, consistent with the terminology in [39].

Generalized Rouse approach: Within the framework of a generalized Rouse approach, β can be related to the static properties for arbitrary fractal dimension d [37,39,53]:

$$\beta = \frac{2}{2+d} \quad (\text{S45})$$

This is derived as follows: at a time-lag t , due to stress propagation, a region of spatial size $\ell \sim t^{\beta/2}$ behaves effectively as a single monomer. Then, the key assumption is the so-called ‘free-draining’ limit, i.e. only local friction on every monomer and no hydrodynamic interactions. Thus, the effective diffusion coefficient D of this region then scales with the number of monomers contained within the region, which is determined by the fractal dimension: $D \sim \ell^{-d}$. Therefore, the MSD of the region is $Dt \sim t^{1-\beta d/2}$, which yields Eq. (S45). Eq. (S45) then yields $\beta = 1/2$ for $d = 2$ and $\beta = 2/5$ for the crumpled chain ($d = 3$).

Zimm model: The Zimm model describes polymers that have a hydrodynamic self-interaction [54], meaning that the monomer beads do not only interact with their nearest neighbors through the springs linking them, but through long-ranged hydrodynamic interactions. Within the Zimm model, the dynamic exponent is independent of the fractal packing dimension d and is given by $\beta = 2/3$.

Relaxation time scaling: To quantify the time-scale on which the cross-over between the two regimes (Eq. (S42) and Eq. (S44)) occurs, we focus on the relaxation time τ . The relaxation time can be estimated as the time taken for the two loci to diffuse their typical distance of separation [39]. In terms of the two-locus MSD, this time scale is therefore given by the intersection of the diffusive part (Eq. (S44)) and the long-time plateau (Eq. (S42)):

$$2\Gamma_2\tau^\beta \sim 2\langle R^2 \rangle \quad (\text{S46})$$

Based on this relationship, we can infer the relaxation times from the experimental two-locus MSD curves, as shown in detail in section 4.1. Furthermore, Eq. (S46) predicts the scaling of the relaxation time with genomic separation for different fractal dimensions for both the generalized Rouse and the Zimm models:

$$\tau^\beta \sim s^{2/d} \quad \rightarrow \quad \tau \sim s^\gamma \quad \text{with } \gamma = 2/(\beta d) \quad (\text{S47})$$

We thus obtain the classical relaxation time scaling for the ideal chain Rouse model:

$$\tau^{1/2} \sim s \quad \rightarrow \quad \tau \sim s^2 \quad (\text{S48})$$

For a crumpled chain described by the generalized Rouse model, both the diffusion exponent and the packing exponent change, and we therefore obtain

$$\tau^{2/5} \sim s^{2/3} \quad \rightarrow \quad \tau \sim s^{5/3} \quad (\text{S49})$$

Thus, the relaxation time exhibits a weaker scaling with genomic separation in the crumpled chain model (exponent ≈ 1.66) than in the ideal chain model (exponent 2). These two exponents are shown as the theoretical predictions in the main text Fig. 4.

We can make the same arguments based on the exponents of the Zimm model for ideal and crumpled chains. Thus, for the ideal chain Zimm model,

$$\tau^{2/3} \sim s \quad \rightarrow \quad \tau \sim s^{3/2} \quad (\text{S50})$$

For a crumpled chain described by the Zimm model, we obtain

$$\tau^{2/3} \sim s^{2/3} \quad \rightarrow \quad \tau \sim s^1 \quad (\text{S51})$$

These various results are summarised in Table S7.

<i>dynamics</i> <i>statics</i>	Rouse	Zimm
general d	$\beta = 2/(2 + d)$ $\gamma = (2 + d)/d$	$\beta = 2/3$ $\gamma = 3/d$
ideal chain $d = 2$	$\beta = 1/2$ $\gamma = 2$	$\beta = 2/3$ $\gamma = 3/2$
crumpled chain $d = 3$	$\beta = 4/5$ $\gamma = 5/3$	$\beta = 2/3$ $\gamma = 1$

Table S7: Overview of exponents β, γ expected for various combinations of statics (ideal/crumpled) and dynamics (Rouse/Zimm).

Two-locus autocorrelation function: Besides the two-locus MSD, a second quantity that quantifies the joint dynamics of two loci based on the interlocus distance vector is the two-locus autocorrelation, given by

$$C_2(t) = \langle \mathbf{R}_{ij}(t_0 + t) \cdot \mathbf{R}_{ij}(t_0) \rangle_{t_0} \quad (\text{S52})$$

The quantities M_2 and C_2 contain the same information since they are directly related to each other through the relationship [26]

$$M_2(t) = 2(C_2(0) - C_2(t)) \quad (\text{S53})$$

However, the function C_2 gives access to the scaling exponents that characterize the approach to equilibration in the long time limit $t \gg \tau$, which are ‘washed out’ in the cross-over to the plateau in M_2 .

Specifically, for C_2 , the short time behaviour ($t \ll \tau$) is determined by the chain size:

$$C_2(t \rightarrow 0) = \langle R^2 \rangle \quad (\text{S54})$$

The asymptotic power-law behavior of the two-locus correlation function in the limit $t \ll \tau$ has been derived based on the generalized Rouse framework [39], predicting that it decays with a power-law whose exponents depend on the fractal dimension:

$$C_2(t) \sim t^{-\lambda} \quad (\text{S55})$$

where

$$\lambda = 2 \frac{d - 1}{2 + d} \quad (\text{S56})$$

which gives $\lambda = 1/2$ for ideal and $\lambda = 4/5$ for crumpled chains. Note that this derivation additionally assumes $s \ll N$, where N is the total length of the chromosome. In our system (*Drosophila* chromosome 2L), $N = 25$ Mb, significantly larger than the typical genomic separations we probe (58 kb – 3.3 Mb). Furthermore, we do not see any signatures of whole chain relaxation in the single-locus MSDs (Fig. S14), suggesting this assumption is valid. Thus, the two-locus autocorrelation can be used to quantify the approach to equilibration of the system, which is separate from the small-time scaling of the two-locus MSD, quantified by exponent β , which is determined by the independent diffusion of the loci.

Finally, we can use the two-locus autocorrelation as an additional way to infer the relaxation times by collapsing the autocorrelations onto a single master curve. Specifically, we expect the correlations to collapse onto the mastercurve [39]

$$C_2(\tilde{t}) \sim s^{-2/d} C_2(ts^{-\gamma}) \quad (\text{S57})$$

where γ is the exponent of the relaxation time, $\tau \sim s^\gamma$. Thus, by quantifying the collapse of C_2 for varying s , we can identify the scaling exponent γ (see section 4.2).

6 Comparison to mESC data

To compare our quantitative results to previous measurements of live imaging of pairs of DNA loci, we make a side-by-side comparison of our data set with that in ref. [26], where CTCF sites in the *Fbn2* locus imaged in mouse embryonic stem cells (mESCs) were tagged with a genomic separation of 515 kb between fluorescent tags (C36 line). We compare our closest genomic separation to this data (595 kb) and find that both average distances and diffusive time scales are much higher in our system. Specifically, while the average distance for mESCs is $\langle R \rangle \approx 0.35\mu\text{m}$, we find $\langle R \rangle \approx 1.05\mu\text{m}$, a factor 3 larger. Furthermore, the two-locus diffusivity $\Gamma_2 = 0.0024\mu\text{m}^2\text{s}^{-1/2}$ for mESCs, and $\Gamma_2 = 0.045\mu\text{m}^2\text{s}^{-1/2}$ in our system, almost 20-fold larger. As a result, despite the larger physical distance between the two loci, the relaxation time is almost an order of magnitude shorter than observed in ref. [26].

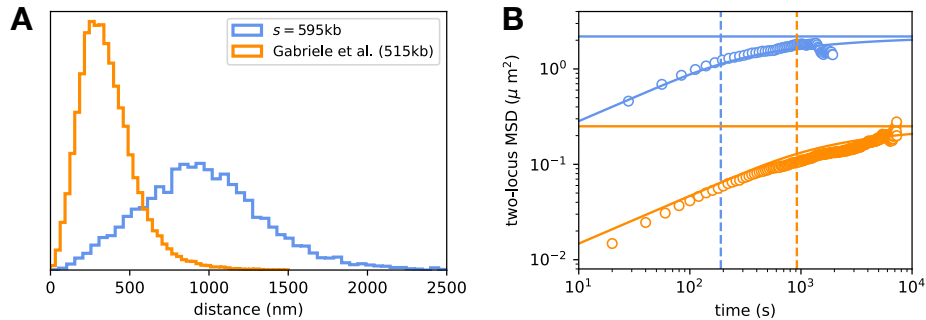


Figure S23: **Two-locus analysis compared to data from ref. [26].** (A) Probability distributions of the inter-locus distances R_{ij} . Blue: our data for $s = 595$ kb (all states), orange: data of CTCF sites in the *Fbn2* locus imaged in mouse embryonic stem cells (mESCs), with a genomic separation of 515 kb (C36 wildtype line) [26]. (B) Localization-error corrected two-locus MSDs for both data sets (open symbols). Solid line: Fit of Eqn. (S28). Solid horizontal line: $2\langle R^2 \rangle$. Dashed vertical line: the fitted value of the relaxation time τ .

7 Code and software

Code and software used in this paper are listed in Table S8.

Name	Reference	URL
DynamicChromosome	[70]	https://github.com/dbrueckner/DynamicChromosome
numpy 1.22.0	[84]	https://numpy.org/
scipy 1.4.1	[85]	https://scipy.org/
matplotlib 3.1.3	[86]	https://matplotlib.org/
tracklib	[26]	https://github.com/SGrosse-Holz/tracklib
Matlab 2020b	—	https://mathworks.com/products/matlab.html

Table S8: List of software used.

Movie description

Supplementary Movies S1-S7

Three-color live imaging of two loci on the second *Drosophila* chromosome separated by increasing genomic distances of {57.8, 81.7, 87.5, 148.7, 189.6, 595.1, 3327.7} kb. The embryo is 2 h old. Movie starts at 27 min in cell cycle 14 and ends at 55 min. Blue spots mark *eve*-MS2 transcription as well as the physical position of the *eve* locus and *eve* enhancers. Green spots are from the *parS* sequence, which marks the location of the reporter construct. Red spots mark transcriptional activity from the PP7 reporter. Scale bar: 5 μm .

References and Notes

1. W. Flemming. *Zellsubstanz, Kern Und Zelltheilung* (Vogel, 1882).
2. R. Milo, R. Phillips, *Cell Biology by the Numbers* (CRC Press, 2015).
3. R. Stadhouders, G. J. Filion, T. Graf, Transcription factors and 3D genome conformation in cell-fate decisions. *Nature* **569**, 345–354 (2019). [doi:10.1038/s41586-019-1182-7](https://doi.org/10.1038/s41586-019-1182-7) [Medline](#)
4. B. van Steensel, E. E. M. Furlong, The role of transcription in shaping the spatial organization of the genome. *Nat. Rev. Mol. Cell Biol.* **20**, 327–337 (2019). [doi:10.1038/s41580-019-0114-6](https://doi.org/10.1038/s41580-019-0114-6) [Medline](#)
5. M. Levine, Transcriptional enhancers in animal development and evolution. *Curr. Biol.* **20**, R754–R763 (2010). [doi:10.1016/j.cub.2010.06.070](https://doi.org/10.1016/j.cub.2010.06.070) [Medline](#)
6. T. K. Kim, R. Shiekhattar, Architectural and functional commonalities between enhancers and promoters. *Cell* **162**, 948–959 (2015). [doi:10.1016/j.cell.2015.08.008](https://doi.org/10.1016/j.cell.2015.08.008) [Medline](#)
7. D. Vernimmen, W. A. Bickmore, The hierarchy of transcriptional activation: From enhancer to promoter. *Trends Genet.* **31**, 696–708 (2015). [doi:10.1016/j.tig.2015.10.004](https://doi.org/10.1016/j.tig.2015.10.004) [Medline](#)
8. H. Chen, M. Levo, L. Barinov, M. Fujioka, J. B. Jaynes, T. Gregor, Dynamic interplay between enhancer-promoter topology and gene activity. *Nat. Genet.* **50**, 1296–1303 (2018). [doi:10.1038/s41588-018-0175-z](https://doi.org/10.1038/s41588-018-0175-z) [Medline](#)
9. B. Tolhuis, R. J. Palstra, E. Splinter, F. Grosveld, W. de Laat, Looping and interaction between hypersensitive sites in the active β -globin locus. *Mol. Cell* **10**, 1453–1465 (2002). [doi:10.1016/S1097-2765\(02\)00781-5](https://doi.org/10.1016/S1097-2765(02)00781-5) [Medline](#)
10. V. V. Uslu, M. Petretich, S. Ruf, K. Langenfeld, N. A. Fonseca, J. C. Marioni, F. Spitz, Long-range enhancers regulating Myc expression are required for normal facial morphogenesis. *Nat. Genet.* **46**, 753–758 (2014). [doi:10.1038/ng.2971](https://doi.org/10.1038/ng.2971) [Medline](#)
11. Y. Zhang, C. H. Wong, R. Y. Birnbaum, G. Li, R. Favaro, C. Y. Ngan, J. Lim, E. Tai, H. M. Poh, E. Wong, F. H. Mulawadi, W. K. Sung, S. Nicolis, N. Ahituv, Y. Ruan, C. L. Wei, Chromatin connectivity maps reveal dynamic promoter-enhancer long-range associations. *Nature* **504**, 306–310 (2013). [doi:10.1038/nature12716](https://doi.org/10.1038/nature12716) [Medline](#)
12. A. Sanyal, B. R. Lajoie, G. Jain, J. Dekker, The long-range interaction landscape of gene promoters. *Nature* **489**, 109–113 (2012). [doi:10.1038/nature11279](https://doi.org/10.1038/nature11279) [Medline](#)
13. Y. Huang, R. Neijts, W. de Laat, How chromosome topologies get their shape: Views from proximity ligation and microscopy methods. *FEBS Lett.* **594**, 3439–3449 (2020). [doi:10.1002/1873-3468.13961](https://doi.org/10.1002/1873-3468.13961) [Medline](#)
14. J. R. Dixon, S. Selvaraj, F. Yue, A. Kim, Y. Li, Y. Shen, M. Hu, J. S. Liu, B. Ren, Topological domains in mammalian genomes identified by analysis of chromatin interactions. *Nature* **485**, 376–380 (2012). [doi:10.1038/nature11082](https://doi.org/10.1038/nature11082) [Medline](#)
15. C. Hou, L. Li, Z. S. Qin, V. G. Corces, Gene density, transcription, and insulators contribute to the partition of the *Drosophila* genome into physical domains. *Mol. Cell* **48**, 471–484 (2012). [doi:10.1016/j.molcel.2012.08.031](https://doi.org/10.1016/j.molcel.2012.08.031) [Medline](#)

16. E. P. Nora, B. R. Lajoie, E. G. Schulz, L. Giorgetti, I. Okamoto, N. Servant, T. Piolot, N. L. van Berkum, J. Meisig, J. Sedat, J. Gribnau, E. Barillot, N. Blüthgen, J. Dekker, E. Heard, Spatial partitioning of the regulatory landscape of the X-inactivation centre. *Nature* **485**, 381–385 (2012). [doi:10.1038/nature11049](https://doi.org/10.1038/nature11049) [Medline](#)
17. T. Sexton, E. Yaffe, E. Kenigsberg, F. Bantignies, B. Leblanc, M. Hoichman, H. Parrinello, A. Tanay, G. Cavalli, Three-dimensional folding and functional organization principles of the *Drosophila* genome. *Cell* **148**, 458–472 (2012). [doi:10.1016/j.cell.2012.01.010](https://doi.org/10.1016/j.cell.2012.01.010) [Medline](#)
18. A. Boija, I. A. Klein, B. R. Sabari, A. Dall’Agnese, E. L. Coffey, A. V. Zamudio, C. H. Li, K. Shrinivas, J. C. Manteiga, N. M. Hannett, B. J. Abraham, L. K. Afeyan, Y. E. Guo, J. K. Rimel, C. B. Fant, J. Schuijers, T. I. Lee, D. J. Taatjes, R. A. Young, Transcription Factors Activate Genes through the Phase-Separation Capacity of Their Activation Domains. *Cell* **175**, 1842–1855.e16 (2018). [doi:10.1016/j.cell.2018.10.042](https://doi.org/10.1016/j.cell.2018.10.042) [Medline](#)
19. W.-K. Cho, J.-H. Spille, M. Hecht, C. Lee, C. Li, V. Grube, I. I. Cisse, Mediator and RNA polymerase II clusters associate in transcription-dependent condensates. *Science* **361**, 412–415 (2018). [doi:10.1126/science.aar4199](https://doi.org/10.1126/science.aar4199) [Medline](#)
20. M. Conte, E. Irani, A. M. Chiariello, A. Abraham, S. Bianco, A. Esposito, M. Nicodemi, Loop-extrusion and polymer phase-separation can co-exist at the single-molecule level to shape chromatin folding. *Nat. Commun.* **13**, 4070 (2022). [doi:10.1038/s41467-022-31856-6](https://doi.org/10.1038/s41467-022-31856-6) [Medline](#)
21. C. S. Osborne, L. Chakalova, K. E. Brown, D. Carter, A. Horton, E. Debrand, B. Goyenechea, J. A. Mitchell, S. Lopes, W. Reik, P. Fraser, Active genes dynamically colocalize to shared sites of ongoing transcription. *Nat. Genet.* **36**, 1065–1071 (2004). [doi:10.1038/ng1423](https://doi.org/10.1038/ng1423) [Medline](#)
22. E. Lieberman-Aiden, N. L. van Berkum, L. Williams, M. Imakaev, T. Ragozy, A. Telling, I. Amit, B. R. Lajoie, P. J. Sabo, M. O. Dorschner, R. Sandstrom, B. Bernstein, M. A. Bender, M. Groudine, A. Gnirke, J. Stamatoyannopoulos, L. A. Mirny, E. S. Lander, J. Dekker, Comprehensive mapping of long-range interactions reveals folding principles of the human genome. *Science* **326**, 289–293 (2009). [doi:10.1126/science.1181369](https://doi.org/10.1126/science.1181369) [Medline](#)
23. O. Symmons, V. V. Uslu, T. Tsujimura, S. Ruf, S. Nassari, W. Schwarzer, L. Ettwiller, F. Spitz, Functional and topological characteristics of mammalian regulatory domains. *Genome Res.* **24**, 390–400 (2014). [doi:10.1101/gr.163519.113](https://doi.org/10.1101/gr.163519.113) [Medline](#)
24. T. J. Stevens, D. Lando, S. Basu, L. P. Atkinson, Y. Cao, S. F. Lee, M. Leeb, K. J. Wohlfahrt, W. Boucher, A. O’Shaughnessy-Kirwan, J. Cramard, A. J. Faure, M. Ralser, E. Blanco, L. Morey, M. Sansó, M. G. S. Palayret, B. Lehner, L. Di Croce, A. Wutz, B. Hendrich, D. Klenerman, E. D. Laue, 3D structures of individual mammalian genomes studied by single-cell Hi-C. *Nature* **544**, 59–64 (2017). [doi:10.1038/nature21429](https://doi.org/10.1038/nature21429) [Medline](#)
25. M. V. Arrastia, J. W. Jachowicz, N. Ollikainen, M. S. Curtis, C. Lai, S. A. Quinodoz, D. A. Selck, R. F. Ismagilov, M. Guttman, Single-cell measurement of higher-order 3D genome organization with scSPRITE. *Nat. Biotechnol.* **40**, 64–73 (2022). [doi:10.1038/s41587-021-00998-1](https://doi.org/10.1038/s41587-021-00998-1) [Medline](#)

26. M. Gabriele, H. B. Brandão, S. Grosse-Holz, A. Jha, G. M. Dailey, C. Cattoglio, T. S. Hsieh, L. Mirny, C. Zechner, A. S. Hansen, Dynamics of CTCF- and cohesin-mediated chromatin looping revealed by live-cell imaging. *Science* **376**, 496–501 (2022). [doi:10.1126/science.abn6583](https://doi.org/10.1126/science.abn6583) [Medline](#)
27. P. Mach, P. I. Kos, Y. Zhan, J. Cramard, S. Gaudin, J. Tünnermann, E. Marchi, J. Eglinger, J. Zuin, M. Kryzhanovska, S. Smallwood, L. Gelman, G. Roth, E. P. Nora, G. Tiana, L. Giorgetti, Cohesin and CTCF control the dynamics of chromosome folding. *Nat. Genet.* **54**, 1907–1918 (2022). [doi:10.1038/s41588-022-01232-7](https://doi.org/10.1038/s41588-022-01232-7) [Medline](#)
28. M. Levo, J. Raimundo, X. Y. Bing, Z. Sisco, P. J. Batut, S. Ryabichko, T. Gregor, M. S. Levine, Transcriptional coupling of distant regulatory genes in living embryos. *Nature* **605**, 754–760 (2022). [doi:10.1038/s41586-022-04680-7](https://doi.org/10.1038/s41586-022-04680-7) [Medline](#)
29. S. Wang, J.-H. Su, B. J. Beliveau, B. Bintu, J. R. Moffitt, C. T. Wu, X. Zhuang, Spatial organization of chromatin domains and compartments in single chromosomes. *Science* **353**, 598–602 (2016). [doi:10.1126/science.aaf8084](https://doi.org/10.1126/science.aaf8084) [Medline](#)
30. B. Bintu, L. J. Mateo, J. H. Su, N. A. Sinnott-Armstrong, M. Parker, S. Kinrot, K. Yamaya, A. N. Boettiger, X. Zhuang, Super-resolution chromatin tracing reveals domains and cooperative interactions in single cells. *Science* **362**, eaau1783 (2018). [doi:10.1126/science.aau1783](https://doi.org/10.1126/science.aau1783) [Medline](#)
31. A. Grosberg, Y. Rabin, S. Havlin, A. Neer, Crumpled globule model of the three-dimensional structure of DNA. *Europhys. Lett.* **23**, 373–378 (1993). [doi:10.1209/0295-5075/23/5/012](https://doi.org/10.1209/0295-5075/23/5/012)
32. A. Yu. Grosberg, S. K. Nechaev, E. I. Shakhnovich, The role of topological constraints in the kinetics of collapse of macromolecules. *J. Phys. (Paris)* **49**, 2095–2100 (1988). [doi:10.1051/jphys:0198800490120209500](https://doi.org/10.1051/jphys:0198800490120209500)
33. L. A. Mirny, The fractal globule as a model of chromatin architecture in the cell. *Chromosome Res.* **19**, 37–51 (2011). [doi:10.1007/s10577-010-9177-0](https://doi.org/10.1007/s10577-010-9177-0) [Medline](#)
34. S. C. Weber, A. J. Spakowitz, J. A. Theriot, Bacterial chromosomal loci move subdiffusively through a viscoelastic cytoplasm. *Phys. Rev. Lett.* **104**, 238102 (2010). [doi:10.1103/PhysRevLett.104.238102](https://doi.org/10.1103/PhysRevLett.104.238102) [Medline](#)
35. J. S. Lucas, Y. Zhang, O. K. Dudko, C. Murre, 3D trajectories adopted by coding and regulatory DNA elements: First-passage times for genomic interactions. *Cell* **158**, 339–352 (2014). [doi:10.1016/j.cell.2014.05.036](https://doi.org/10.1016/j.cell.2014.05.036) [Medline](#)
36. J. M. Alexander, J. Guan, B. Li, L. Maliskova, M. Song, Y. Shen, B. Huang, S. Lomvardas, O. D. Weiner, Live-cell imaging reveals enhancer-dependent *Sox2* transcription in the absence of enhancer proximity. *eLife* **8**, e41769 (2019). [doi:10.7554/eLife.41769](https://doi.org/10.7554/eLife.41769) [Medline](#)
37. M. V. Tamm, L. I. Nazarov, A. A. Gavrilov, A. V. Chertovich, Anomalous diffusion in fractal globules. *Phys. Rev. Lett.* **114**, 178102 (2015). [doi:10.1103/PhysRevLett.114.178102](https://doi.org/10.1103/PhysRevLett.114.178102) [Medline](#)
38. S. Shinkai, T. Nozaki, K. Maeshima, Y. Togashi, Dynamic nucleosome movement provides structural information of topological chromatin domains in living human cells. *PLOS Comput. Biol.* **12**, e1005136 (2016). [doi:10.1371/journal.pcbi.1005136](https://doi.org/10.1371/journal.pcbi.1005136) [Medline](#)

39. K. E. Polovnikov, M. Gherardi, M. Cosentino-Lagomarsino, M. V. Tamm, Fractal folding and medium viscoelasticity contribute jointly to chromosome dynamics. *Phys. Rev. Lett.* **120**, 088101 (2018). [doi:10.1103/PhysRevLett.120.088101](https://doi.org/10.1103/PhysRevLett.120.088101) [Medline](#)
40. M. Nicodemi, A. Pombo, Models of chromosome structure. *Curr. Opin. Cell Biol.* **28**, 90–95 (2014). [doi:10.1016/j.ceb.2014.04.004](https://doi.org/10.1016/j.ceb.2014.04.004) [Medline](#)
41. N. Khanna, Y. Zhang, J. S. Lucas, O. K. Dudko, C. Murre, Chromosome dynamics near the sol-gel phase transition dictate the timing of remote genomic interactions. *Nat. Commun.* **10**, 2771 (2019). [doi:10.1038/s41467-019-10628-9](https://doi.org/10.1038/s41467-019-10628-9) [Medline](#)
42. T. Germier, S. Kocanova, N. Walther, A. Bancaud, H. A. Shaban, H. Sellou, A. Z. Politi, J. Ellenberg, F. Gallardo, K. Bystricky, Real-time imaging of a single gene reveals transcription-initiated local confinement. *Biophys. J.* **113**, 1383–1394 (2017). [doi:10.1016/j.bpj.2017.08.014](https://doi.org/10.1016/j.bpj.2017.08.014) [Medline](#)
43. B. Gu, T. Swigut, A. Spencley, M. R. Bauer, M. Chung, T. Meyer, J. Wysocka, Transcription-coupled changes in nuclear mobility of mammalian cis-regulatory elements. *Science* **359**, 1050–1055 (2018). [doi:10.1126/science.aao3136](https://doi.org/10.1126/science.aao3136) [Medline](#)
44. J. Zuin, G. Roth, Y. Zhan, J. Cramard, J. Redolfi, E. Piskadlo, P. Mach, M. Kryzhanovska, G. Tihanyi, H. Kohler, M. Eder, C. Leemans, B. van Steensel, P. Meister, S. Smallwood, L. Giorgetti, Nonlinear control of transcription through enhancer-promoter interactions. *Nature* **604**, 571–577 (2022). [doi:10.1038/s41586-022-04570-y](https://doi.org/10.1038/s41586-022-04570-y) [Medline](#)
45. S. V. Ulianov, V. V. Zakharova, A. A. Galitsyna, P. I. Kos, K. E. Polovnikov, I. M. Flyamer, E. A. Mikhaleva, E. E. Khrameeva, D. Germini, M. D. Logacheva, A. A. Gavrilov, A. S. Gorsky, S. K. Nechaev, M. S. Gelfand, Y. S. Vassetzky, A. V. Chertovich, Y. Y. Shevelyov, S. V. Razin, Order and stochasticity in the folding of individual *Drosophila* genomes. *Nat. Commun.* **12**, 41 (2021). [doi:10.1038/s41467-020-20292-z](https://doi.org/10.1038/s41467-020-20292-z) [Medline](#)
46. B. L. Hua, T. L. Orr-Weaver, DNA replication control during *Drosophila* development: Insights into the onset of S phase, replication initiation, and fork progression. *Genetics* **207**, 29–47 (2017). [doi:10.1534/genetics.115.186627](https://doi.org/10.1534/genetics.115.186627) [Medline](#)
47. B. Avşaroğlu, G. Bronk, S. Gordon-Messer, J. Ham, D. A. Bressan, J. E. Haber, J. Kondev, Effect of chromosome tethering on nuclear organization in yeast. *PLOS ONE* **9**, e102474 (2014). [doi:10.1371/journal.pone.0102474](https://doi.org/10.1371/journal.pone.0102474) [Medline](#)
48. J. Dekker, M. A. Marti-Renom, L. A. Mirny, Exploring the three-dimensional organization of genomes: Interpreting chromatin interaction data. *Nat. Rev. Genet.* **14**, 390–403 (2013). [doi:10.1038/nrg3454](https://doi.org/10.1038/nrg3454) [Medline](#)
49. L. Barinov, S. Ryabichko, W. Bialek, T. Gregor, Transcription-dependent spatial organization of a gene locus. [arXiv:2012.15819 \[q-bio.MN\]](https://arxiv.org/abs/2012.15819) (2020).
50. B. Zoller, S. C. Little, T. Gregor, Diverse spatial expression patterns emerge from unified kinetics of transcriptional bursting. *Cell* **175**, 835–847.e25 (2018). [doi:10.1016/j.cell.2018.09.056](https://doi.org/10.1016/j.cell.2018.09.056) [Medline](#)
51. A. Rosa, N. B. Becker, R. Everaers, Looping probabilities in model interphase chromosomes. *Biophys. J.* **98**, 2410–2419 (2010). [doi:10.1016/j.bpj.2010.01.054](https://doi.org/10.1016/j.bpj.2010.01.054) [Medline](#)

52. J. D. Halverson, W. B. Lee, G. S. Grest, A. Y. Grosberg, K. Kremer, Molecular dynamics simulation study of nonconcatenated ring polymers in a melt. I. Statics. *J. Chem. Phys.* **134**, 204904 (2011). [doi:10.1063/1.3587137](https://doi.org/10.1063/1.3587137) [Medline](#)
53. P. G. De Gennes, Dynamics of entangled polymer solutions. I. The Rouse Model. *Macromolecules* **9**, 587–593 (1976). [doi:10.1021/ma60052a011](https://doi.org/10.1021/ma60052a011)
54. M. Rubinstein, R. H. Colby, *Polymer Physics* (Oxford Univ. Press, 2003).
55. T. J. Lampo, A. S. Kennard, A. J. Spakowitz, Physical modeling of dynamic coupling between chromosomal loci. *Biophys. J.* **110**, 338–347 (2016). [doi:10.1016/j.bpj.2015.11.3520](https://doi.org/10.1016/j.bpj.2015.11.3520) [Medline](#)
56. A. Kaushal, G. Mohana, J. Dorier, I. Özdemir, A. Omer, P. Cousin, A. Semenova, M. Taschner, O. Dergai, F. Marzetta, C. Iseli, Y. Eliaz, D. Weisz, M. S. Shamim, N. Guex, E. Lieberman Aiden, M. C. Gambetta, CTCF loss has limited effects on global genome architecture in *Drosophila* despite critical regulatory functions. *Nat. Commun.* **12**, 1011 (2021). [doi:10.1038/s41467-021-21366-2](https://doi.org/10.1038/s41467-021-21366-2) [Medline](#)
57. G. Wilemski, M. Fixman, Diffusion-controlled intrachain reactions of polymers. I Theory. *J. Chem. Phys.* **60**, 866–877 (1974). [doi:10.1063/1.1681162](https://doi.org/10.1063/1.1681162)
58. A. Szabo, K. Schulten, Z. Schulten, First passage time approach to diffusion controlled reactions. *J. Chem. Phys.* **72**, 4350–4357 (1980). [doi:10.1063/1.439715](https://doi.org/10.1063/1.439715)
59. M. Fujioka, H. Mistry, P. Schedl, J. B. Jaynes, Determinants of chromosome architecture: Insulator pairing in cis and in trans. *PLOS Genet.* **12**, e1005889 (2016). [doi:10.1371/journal.pgen.1005889](https://doi.org/10.1371/journal.pgen.1005889) [Medline](#)
60. R. Bruinsma, A. Y. Grosberg, Y. Rabin, A. Zidovska, Chromatin hydrodynamics. *Biophys. J.* **106**, 1871–1881 (2014). [doi:10.1016/j.bpj.2014.03.038](https://doi.org/10.1016/j.bpj.2014.03.038) [Medline](#)
61. M. M. Tortora, H. Salari, D. Jost, Chromosome dynamics during interphase: A biophysical perspective. *Curr. Opin. Genet. Dev.* **61**, 37–43 (2020). [doi:10.1016/j.gde.2020.03.001](https://doi.org/10.1016/j.gde.2020.03.001) [Medline](#)
62. R. Kawamura, L. H. Pope, M. O. Christensen, M. Sun, K. Terekhova, F. Boege, C. Mielke, A. H. Andersen, J. F. Marko, Mitotic chromosomes are constrained by topoisomerase II-sensitive DNA entanglements. *J. Cell Biol.* **188**, 653–663 (2010). [doi:10.1083/jcb.200910085](https://doi.org/10.1083/jcb.200910085) [Medline](#)
63. A. Rosa, R. Everaers, Structure and dynamics of interphase chromosomes. *PLOS Comput. Biol.* **4**, e1000153 (2008). [doi:10.1371/journal.pcbi.1000153](https://doi.org/10.1371/journal.pcbi.1000153) [Medline](#)
64. M. Barbieri, M. Chotalia, J. Fraser, L.-M. Lavitas, J. Dostie, A. Pombo, M. Nicodemi, Complexity of chromatin folding is captured by the strings and binders switch model. *Proc. Natl. Acad. Sci. U.S.A.* **109**, 16173–16178 (2012). [doi:10.1073/pnas.1204799109](https://doi.org/10.1073/pnas.1204799109) [Medline](#)
65. L. Giorgetti, R. Galupa, E. P. Nora, T. Piolot, F. Lam, J. Dekker, G. Tian, E. Heard, Predictive polymer modeling reveals coupled fluctuations in chromosome conformation and transcription. *Cell* **157**, 950–963 (2014). [doi:10.1016/j.cell.2014.03.025](https://doi.org/10.1016/j.cell.2014.03.025) [Medline](#)

66. L. Liu, G. Shi, D. Thirumalai, C. Hyeon, Chain organization of human interphase chromosome determines the spatiotemporal dynamics of chromatin loci. *PLOS Comput. Biol.* **14**, e1006617 (2018). [doi:10.1371/journal.pcbi.1006617](https://doi.org/10.1371/journal.pcbi.1006617) [Medline](#)
67. A. Buckle, C. A. Brackley, S. Boyle, D. Marenduzzo, N. Gilbert, Polymer simulations of heteromorphic chromatin predict the 3D folding of complex genomic loci. *Mol. Cell* **72**, 786–797.e11 (2018). [doi:10.1016/j.molcel.2018.09.016](https://doi.org/10.1016/j.molcel.2018.09.016) [Medline](#)
68. C. A. Brackley, D. Marenduzzo, N. Gilbert, Mechanistic modeling of chromatin folding to understand function. *Nat. Methods* **17**, 767–775 (2020). [doi:10.1038/s41592-020-0852-6](https://doi.org/10.1038/s41592-020-0852-6) [Medline](#)
69. H. Salari, M. Di Stefano, D. Jost, Spatial organization of chromosomes leads to heterogeneous chromatin motion and drives the liquid- or gel-like dynamical behavior of chromatin. *Genome Res.* **32**, 28–43 (2022). [doi:10.1101/gr.275827.121](https://doi.org/10.1101/gr.275827.121) [Medline](#)
70. D. B. Brückner, B. Zoller, dbrueckner/DynamicChromosome: initial release, Zenodo (2023); <https://zenodo.org/record/7926778>.
71. D. B. Brückner, H. Chen, L. Barinov, B. Zoller, T. Gregor, Trajectory data for: Stochastic motion and transcriptional dynamics of pairs of distal DNA loci on a compacted chromosome, Zenodo (2023); <https://zenodo.org/record/7616203>.
72. S. J. Gratz, F. P. Ukken, C. D. Rubinstein, G. Thiede, L. K. Donohue, A. M. Cummings, K. M. O’Connor-Giles, Highly specific and efficient CRISPR/Cas9-catalyzed homology-directed repair in *Drosophila*. *Genetics* **196**, 961–971 (2014). [doi:10.1534/genetics.113.160713](https://doi.org/10.1534/genetics.113.160713) [Medline](#)
73. K. J. T. Venken, K. L. Schulze, N. A. Haelterman, H. Pan, Y. He, M. Evans-Holm, J. W. Carlson, R. W. Levis, A. C. Spradling, R. A. Hoskins, H. J. Bellen, MiMIC: A highly versatile transposon insertion resource for engineering *Drosophila melanogaster* genes. *Nat. Methods* **8**, 737–743 (2011). [doi:10.1038/nmeth.1662](https://doi.org/10.1038/nmeth.1662) [Medline](#)
74. H. Chen, Z. Xu, C. Mei, D. Yu, S. Small, A system of repressor gradients spatially organizes the boundaries of Bicoid-dependent target genes. *Cell* **149**, 618–629 (2012). [doi:10.1016/j.cell.2012.03.018](https://doi.org/10.1016/j.cell.2012.03.018) [Medline](#)
75. H. Chen, T. Gregor, “Using RNA tags for multicolor live imaging of chromatin loci and transcription in *Drosophila* embryos,” in *RNA Tagging: Methods and Protocols*, M. Heinlein, Ed. (Springer, 2020), pp. 373–384.
76. J. O. Dubuis, G. Tkacik, E. F. Wieschaus, T. Gregor, W. Bialek, Positional information, in bits. *Proc. Natl. Acad. Sci. U.S.A.* **110**, 16301–16308 (2013). [doi:10.1073/pnas.1315642110](https://doi.org/10.1073/pnas.1315642110) [Medline](#)
77. N. Otsu, A threshold selection method from gray-level histograms. *IEEE Trans. Syst. Man Cybern.* **9**, 62–66 (1979). [doi:10.1109/TSMC.1979.4310076](https://doi.org/10.1109/TSMC.1979.4310076)
78. L. R. Rabiner, A tutorial on hidden Markov models and selected applications in speech recognition. *Proc. IEEE* **77**, 257–286 (1989). [doi:10.1109/5.18626](https://doi.org/10.1109/5.18626)
79. W. K. Hastings, Monte Carlo sampling methods using Markov chains and their applications. *Biometrika* **57**, 97–109 (1970). [doi:10.1093/biomet/57.1.97](https://doi.org/10.1093/biomet/57.1.97)

80. D. T. Gillespie, Stochastic simulation of chemical kinetics. *Annu. Rev. Phys. Chem.* **58**, 35–55 (2007). [doi:10.1146/annurev.physchem.58.032806.104637](https://doi.org/10.1146/annurev.physchem.58.032806.104637) [Medline](#)
81. E. L. Kaplan, P. Meier, Nonparametric estimation from incomplete observations. *J. Am. Stat. Assoc.* **53**, 457–481 (1958). [doi:10.1080/01621459.1958.10501452](https://doi.org/10.1080/01621459.1958.10501452)
82. B. Efron, Bootstrap methods: Another look at the jackknife. *Ann. Stat.* **7**, 1–26 (1979). [doi:10.1214/aos/1176344552](https://doi.org/10.1214/aos/1176344552)
83. B. Efron, R. J. Tibshirani, *An Introduction to the Bootstrap* (CRC Press, 1994).
84. C. R. Harris, K. J. Millman, S. J. van der Walt, R. Gommers, P. Virtanen, D. Cournapeau, E. Wieser, J. Taylor, S. Berg, N. J. Smith, R. Kern, M. Picus, S. Hoyer, M. H. van Kerkwijk, M. Brett, A. Haldane, J. F. Del Río, M. Wiebe, P. Peterson, P. Gérard-Marchant, K. Sheppard, T. Reddy, W. Weckesser, H. Abbasi, C. Gohlke, T. E. Oliphant, Array programming with NumPy. *Nature* **585**, 357–362 (2020). [doi:10.1038/s41586-020-2649-2](https://doi.org/10.1038/s41586-020-2649-2) [Medline](#)
85. P. Virtanen, R. Gommers, T. E. Oliphant, M. Haberland, T. Reddy, D. Cournapeau, E. Burovski, P. Peterson, W. Weckesser, J. Bright, S. J. van der Walt, M. Brett, J. Wilson, K. J. Millman, N. Mayorov, A. R. J. Nelson, E. Jones, R. Kern, E. Larson, C. J. Carey, Í. Polat, Y. Feng, E. W. Moore, J. VanderPlas, D. Laxalde, J. Perktold, R. Cimrman, I. Henriksen, E. A. Quintero, C. R. Harris, A. M. Archibald, A. H. Ribeiro, F. Pedregosa, P. van Mulbregt, A. Vijaykumar, A. P. Bardelli, A. Rothberg, A. Hilboll, A. Kloeckner, A. Scopatz, A. Lee, A. Rokem, C. N. Woods, C. Fulton, C. Masson, C. Häggström, C. Fitzgerald, D. A. Nicholson, D. R. Hagen, D. V. Pasechnik, E. Olivetti, E. Martin, E. Wieser, F. Silva, F. Lenders, F. Wilhelm, G. Young, G. A. Price, G.-L. Ingold, G. E. Allen, G. R. Lee, H. Audren, I. Probst, J. P. Dietrich, J. Silterra, J. T. Webber, J. Slavič, J. Nothman, J. Buchner, J. Kulick, J. L. Schönberger, J. V. de Miranda Cardoso, J. Reimer, J. Harrington, J. L. C. Rodríguez, J. Nunez-Iglesias, J. Kuczynski, K. Tritz, M. Thoma, M. Neville, M. Kümmerer, M. Bolingbroke, M. Tartre, M. Pak, N. J. Smith, N. Nowaczyk, N. Shebanov, O. Pavlyk, P. A. Brodtkorb, P. Lee, R. T. McGibbon, R. Feldbauer, S. Lewis, S. Tygier, S. Sievert, S. Vigna, S. Peterson, S. More, T. Pudlik, T. Oshima, T. J. Pingel, T. P. Robitaille, T. Spura, T. R. Jones, T. Cera, T. Leslie, T. Zito, T. Krauss, U. Upadhyay, Y. O. Halchenko, Y. Vázquez-Baeza; SciPy 1.0 Contributors, SciPy 1.0: Fundamental algorithms for scientific computing in Python. *Nat. Methods* **17**, 261–272 (2020). [doi:10.1038/s41592-019-0686-2](https://doi.org/10.1038/s41592-019-0686-2) [Medline](#)
86. J. D. Hunter, Matplotlib: A 2D Graphics Environment. *Comput. Sci. Eng.* **9**, 90–95 (2007). [doi:10.1109/MCSE.2007.55](https://doi.org/10.1109/MCSE.2007.55)